

# We are IntechOpen, the world's leading publisher of Open Access books Built by scientists, for scientists

6,900

Open access books available

185,000

International authors and editors

200M

Downloads

Our authors are among the

154

Countries delivered to

TOP 1%

most cited scientists

12.2%

Contributors from top 500 universities



WEB OF SCIENCE™

Selection of our books indexed in the Book Citation Index  
in Web of Science™ Core Collection (BKCI)

Interested in publishing with us?  
Contact [book.department@intechopen.com](mailto:book.department@intechopen.com)

Numbers displayed above are based on latest data collected.  
For more information visit [www.intechopen.com](http://www.intechopen.com)



---

# Nanostructured State-of-the-Art Thermoelectric Materials Prepared by Straight-Forward Arc-Melting Method

---

Federico Serrano-Sánchez, Mouna Gharsallah,  
Julián Bermúdez, Félix Carrascoso,  
Norbert M. Nemes, Oscar J. Dura,  
Marco A. López de la Torre, José L. Martínez,  
María T. Fernández-Díaz and José A. Alonso

Additional information is available at the end of the chapter

<http://dx.doi.org/10.5772/65115>

---

## Abstract

Thermoelectric materials constitute an alternative to harvest sustainable energy from waste heat. Among the most commonly utilized thermoelectric materials, we can mention  $\text{Bi}_2\text{Te}_3$  (hole and electron conductivity type),  $\text{PbTe}$  and recently reported  $\text{SnSe}$  intermetallic alloys. We review recent results showing that all of them can be readily prepared in nanostructured form by arc-melting synthesis, yielding mechanically robust pellets of highly oriented polycrystals. These materials have been characterized by neutron powder diffraction (NPD), scanning electron microscopy (SEM) and electronic and thermal transport measurements. Analysis of NPD patterns demonstrates near-perfect stoichiometry of above-mentioned alloys and fair amount of anharmonicity of chemical bonds. SEM analysis shows stacking of nanosized sheets, each of them presumably single-crystalline, with large surfaces parallel to layered slabs. This nanostructuring affects notably thermoelectric properties, involving many surface boundaries (interfaces), which are responsible for large phonon scattering factors, yielding low thermal conductivity. Additionally, we describe homemade apparatus developed for the simultaneous measurement of Seebeck coefficient and electric conductivity at elevated temperatures.

**Keywords:** thermoelectrics, nanostructuring, lattice thermal conductivity, thermopower, neutron powder diffraction

---

## 1. Introduction

Thermoelectric materials possess the remarkable capability to transform temperature differences between two ends of a material sample directly and reversibly into a electrical potential difference. Waste heat recovery, which implies around 70% of primary energy production, exploited as a new source of power generation, could mean significant progress worldwide [1, 2]. Thermoelectric generators are able to perform this task, but currently they are not yet cost-effective. Several advantages featured by thermoelectric power generation devices, such as the absence of moving parts, reliability, endurance, quiet operation and no pollutant emission, make these devices valuable from an energy and environmental point of view and useful in a wide range of applications.

The dimensionless figure of merit  $ZT = (S^2 \sigma)T/k$ , where  $S$  stands for Seebeck coefficient,  $\sigma$  is the electrical conductivity and  $\kappa$  is the total thermal conductivity, evaluates thermoelectric performance of materials and serves as a reference value in thermoelectric materials research [3–8]. Maximization of  $ZT$  requires high Seebeck coefficient and low electrical resistivity and thermal conductivity values. This physical value is closely linked to the power generation efficiency of thermoelectric devices:

$$\varepsilon = \frac{T_H - T_c}{T_H} \frac{\sqrt{1 + ZT_M} - 1}{\sqrt{1 + ZT_M} + \frac{T_c}{T_H}}, \quad (1)$$

where  $T_H$ ,  $T_c$  and  $T_M$  are the temperature of the hot and cold ends and the average temperature. From this, we can abstract, that larger mean  $ZT$  along with larger temperature differences return better conversion efficiencies. Current commercial devices based on BiTe alloys reach efficiencies of ~6%, while new materials based on recent advances to improve  $ZT$  are expected to reach ~12–17%. These approaches are mainly focused on lowering lattice thermal conductivity by bulk nanostructuring and enhancing the power factor,  $S^2\sigma$ , by band engineering.

Experiments with nanostructured thermoelectric materials prove that highly efficient thermoelectric energy conversion could be forthcoming [9, 10]. Bulk samples, containing nanoscale constituents or inhomogeneity, exhibit enhanced thermoelectric phenomena, which are connected with the latest advances in optimizing thermoelectric figure of merit. Materials featuring these characteristics have been found among compounds, where nano-inclusions are inherently formed by using preparation methods to induce the nanostructured morphology. The main effect of nanostructuring is to affect the lattice thermal conductivity. Phonons are effectively scattered, when separation of defects or grain-sizes is similar to phonons' mean-free path. Consequently, bearing in mind the difference in electronic scattering length, structural unit-cells, comparable in size to heat carrying phonon wavelength, will improve the performance. On the other hand, quantum confinement effects could allow to treat  $S$ ,  $\sigma$  and  $k$  quasi-independently and achieve higher power factors, defined as  $S^2\sigma$  product [10–14].

Usually, thermoelectric nanocomposites are prepared initially and then assembled into bulk solids. Several methods for nanostructuring bulk materials have been developed; the most commonly used are spark plasma sintering (SPS), hot pressing, ball milling and wet chemical reactions [15]. All of them present different advantages and disadvantages, but they share drawbacks of long reaction and sample preparation times. For instance, it is expected, that the SPS method will be very beneficial for the reduction in lattice thermal conductivity due to retention of low-dimensional grains. On the other hand, it requires long annealing times and, as expected, results in more pronounced equiaxed morphology of powder particles with decrease in their size [16]. Chemical methods are convenient in terms of particle size, shape and crystallinity; nevertheless, removal of insulating organic capping ligands from nanocrystals is essential before consolidation into bulk pellets, and most of the chemically prepared materials present lower ZT values due to unsuitable charge carriers' concentrations and low intergranular connectivity achieved during compaction [17, 18].

Our present work deals with a straightforward and fast technique based on arc-melting synthesis. We have been able to prepare by this technique different families of thermoelectric materials including  $\text{Bi}_{2-x}\text{Sb}_x\text{Te}_3$  and  $\text{Bi}_2(\text{Te}_{1-x}\text{Se}_x)_3$  alloys, SnSe and related alloys, PbTe and GeSe compounds [19–21]. This method yields highly nanostructured samples prepared in really short times, which require no further processing and are directly implementable into devices. Highly oriented polycrystalline pellets are obtained with extremely low thermal conductivity, probably linked to the nanostructured nature of polycrystalline domains. This chapter describes synthesis by arc-melting and structural and thermoelectric characterization of these materials. Structural characterization has been carried out by X-ray diffraction (XRD) and neutron powder diffraction (NPD), which complements the study of thermoelectric properties and is used as the basis for density functional theory (DFT) calculations. Therefore, we review transport results of various bismuth telluride and tin selenide-related alloys, as well as, some other alloys.  $\text{Bi}_2\text{Te}_3$  forms the basis for the most widely used thermoelectrics near room temperature. Arc-melting is a good technique affording rapid production with various doping and alloying. But how good is the resulting material? Thermoelectric property measurements by various procedures can reveal it.

## 2. Experimental section

### 2.1. Preparation by arc-melting

Intermetallic alloys of different above-mentioned families were prepared in an Edmund Buhler Compact Arc Melter MAM-1 (**Figure 1a**). Stoichiometric amounts of grinded mixture of reacting elements were pelletized in a glove box. Pellets were molten under Ar atmosphere in water-cooled Cu crucible (**Figure 1b**), leading to intermetallic ingots (**Figure 1c**), which can be ground to powder for structural characterization or cut with a diamond saw in bar-shaped samples for transport measurements. Complete characterization of these novel materials has included structural study by XRD and NPD and detailed examination of thermoelectric parameters.

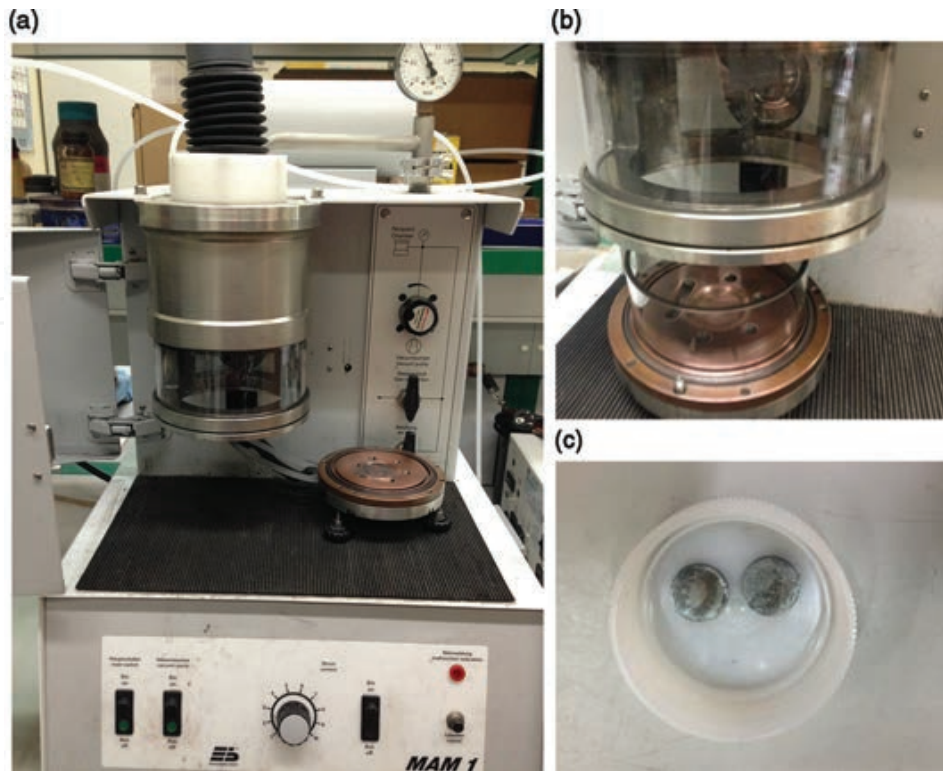


**Figure 1.** (a) Compact arc-melting furnace utilized for synthesis of nanostructured materials. (b) Water-cooled copper crucible, where sample can be quenched after melting process. (c) Typical aspect of as-grown ingots of intermetallic alloys.

## 2.2. Structural characterization

Initial characterization of products was carried out by laboratory XRD ( $\text{Cu K}\alpha$ ,  $\lambda = 1.5406 \text{ \AA}$ ). NPD diagrams were collected either at HRPT diffractometer of SINQ (The Swiss Spallation Neutron Source) spallation source at Paul Scherrer Institut or at D2B high-resolution diffractometer at Institut Laue-Langevin, Grenoble. Patterns were collected at room temperature with a wavelength of  $1.494 \text{ \AA}$  (HRPT) or  $1.594 \text{ \AA}$  (D2B). The high-flux mode was used ( $\Delta d/d \approx 5 \times 10^{-4}$ ); typical collection time was 2 h. For some selected samples ( $\text{Sn}_{0.8}\text{Ge}_{0.2}\text{Se}$ ), temperature-dependent NPD experiment was also carried out at D2B diffractometer. About 2 g of the sample was contained in a vanadium can and placed in the isothermal zone of the furnace with a vanadium resistor operating under vacuum ( $P_{\text{O}_2} \approx 10^{-6} \text{ torr}$ ). Measurements were carried out upon heating at 25, 200, 420 and  $580^\circ\text{C}$ , and NPD data were collected in diffractometer D2B. Diffraction data were analyzed by Rietveld method with FULLPROF program [22]. Line shape of diffraction peaks was generated by pseudo-Voigt function. The following parameters were refined: background points, zero shift, half-width, pseudo-Voigt, scale factor and unit-cell parameters. Positional and occupancy factors and anisotropic displacement factors were also refined for NPD data. Coherent scattering lengths for Bi, Te, Sn, Ge and Se were 8.532, 5.800, 6.225, 8.185 and 7.970 fm, respectively. A preferred orientation correction was applied, considering platelets perpendicular to the [001] for  $\text{Bi}_2\text{Te}_3$ -related alloys and the [100] direction for SnSe-related alloys.

### 2.3. Microstructural characterization

Surface texture of as-grown pellets is studied by field emission SEM (FE-SEM) in ZEISS 55 model. FE-SEM provides very focused energy electron beam, which improves greatly the spatial resolution and allows working at very low potentials, (from 0.02 to 5 kV); this helps to minimize effects of charge load on nonconductive samples and to avoid any damage to electron beam sensitive samples. It offers typical SEM image of surface topography of the sample with large depth of field. It is best suited for middle and low resolutions with high acceleration potential. It is mainly used to browse with low magnification looking for points of interest and to study samples with much topographical information. It also carries a secondary electron detector in lens: located inside the electron column, and it works with low-energy secondary electrons and offers higher resolution images. It is very sensitive to surface characteristics of the sample, so it is very suitable for surface characterization of any material.

### 2.4. Transport measurements

#### 2.4.1. Physical properties measurement system (PPMS)

Three basic properties of thermoelectric materials (Seebeck coefficient, electrical resistivity and thermal conductivity) can be characterized simultaneously over a broad temperature range, between 2 and 400 K, by the thermal transport option (TTO) of the physical properties measurement system (PPMS) of Quantum Design Inc. This system allows for four electrical and thermal contacts with the sample. It uses two small thin-film temperature sensors (Cernox) mounted on small brass holders to measure both voltage and temperature drop across the sample. It uses another small brass piece with 2 kOhm resistive chip heater both to inject electrical current for resistivity measurement and to supply a known amount of heating power for Seebeck and thermal conductivity measurements. The fourth contact of the samples is the large brass baseplate of the sample holder, which thermally anchors it to the cryostat.

Measurements are carried out as follows: we use bar-shaped samples with  $10 \times 3 \times 2 \text{ mm}^3$  dimensions, prepared either by directly cutting from as-prepared ingots or by directly cold-pressing it after arc-melting in a properly shaped die. Four copper leads are wrapped around the bar and then fixed with silver epoxy. We use the following thermal protocol: cool the sample from 300 K to low temperature (either 2 K or 10 K), then warm it to 395 K and then cool it again to base temperature. We use slow sweep rate of 0.3 K/min (over 2 days for each sample) and gather data continuously. Electrical resistivity is measured by applying sinusoidal current with typical frequency of 17 Hz and amplitude between 10  $\mu\text{A}$  and 10 mA. Seebeck coefficient is then measured by establishing a temperature gradient of typically 3% of the sample sink temperature. Here, the only important source of experimental error may arise from the fact, that Cernox temperature sensors are not touching the sample directly, but are thermally connected to it via a few millimeter-length of copper wires. Thermal conductivity is measured by dynamically modeling the temperature gradient on the sample between two Cernox sensors as known heater power (between 10  $\mu\text{W}$  and 50 mW, adjusted to achieve 3% gradient) is supplied, and then removed, to one end of the sample. Above  $\sim 150 \text{ K}$ , errors related to radiative heat losses become important. These are ameliorated to a certain extent by careful application

of the correction software of TTO. Another, less important, source of heat losses is conduction through copper wires of voltage/temperature gradient leads. Finally, convective heat losses are minimized by the high vacuum option of PPMS, establishing pressure below  $10^{-5}$  torr.

For Hall coefficient measurements, we use thin pellets (~1 mm thick, 10 mm diameter) in van der Pauw geometry, with four contacts placed along the perimeter, and pass a DC current with alternating sign to eliminate thermoelectric voltages along diagonal. Measured voltage is still dominated by ohmic resistance, which is then removed by comparing values obtained in large positive and negative magnetic fields.

#### 2.4.2. High-temperature Seebeck coefficient measured in micro-miniature refrigerator (MMR) device

Seebeck coefficient is the ratio of voltage difference produced from applied temperature gradient. In principle, this concept is easy to understand, and one might think that this thermoelectric property is easy to measure. However, it can be difficult to evaluate [23, 24]. Basically, a temperature gradient is established between hot and cold ends of the sample and then the voltage drop, appearing between them, is measured. If the temperature gradient is kept constant during measurement, the method is called steady-state method.

Here we describe a method used by the commercial system of MMR Technologies Inc. (MMR device). This system allows measuring Seebeck coefficient of semiconductors and metals between 70 and 730 K. This method employs two pairs of thermocouples. One pair is formed by junctions of copper and reference material (constantan) with a well-known value of Seebeck coefficient. The other pair is formed of junctions of copper and sample, in which Seebeck coefficient is to be determined (**Figure 2a**). This method requires that both materials, reference and sample, have similar thermal conductance in order to ensure similar thermal transport through both of them. Thus, constantan wires with different diameters are used as a reference to allow evaluating materials with very different thermal conductivities.

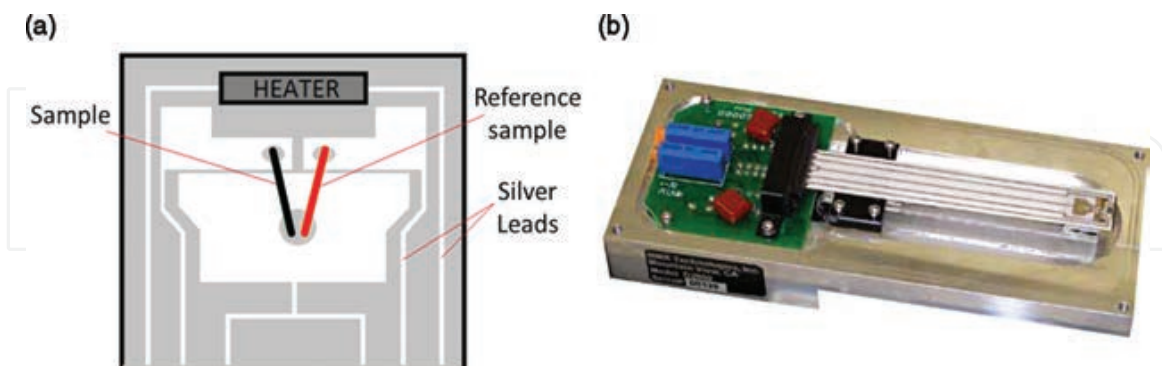


**Figure 2.** (a) Seebeck thermal stage supplied by MMR technologies. Black line indicates place of unknown sample and red line indicates that of reference sample. (b) Chamber with refrigerator, which provides temperature range between 70 and 730 K.

Another interesting characteristic of the method provided by MMR system is the double reference measurement technique, which gives more accurate and reproducible results. By using this feature, the equipment subtracts any instrumental offset voltage due to thermo-

voltage effects from wires or connections. Different stages, made up of alumina or polyamide, allow covering a broad temperature range of measurement from 70 to 730 K (**Figure 2a and b**).

### 2.4.3. High-temperature transport device: high-temperature Seebeck measurements in homemade apparatus

As commented above, measurement of Seebeck coefficient seems like one of the less challenging tasks: create temperature gradient, measure voltage ... What could be simpler? Yet, at elevated temperatures, this poses a challenge, mainly due to large, hard to control, temperature gradients. The largest systematic errors arise from the fact, that it is virtually impossible to detect temperatures at exactly the same spot where voltage difference is measured. Additional difficulty is strong chemical and metallurgic reactivity of typical thermoelectric materials at temperatures above a few hundred degree celsius, limiting the choice of building blocks for any instrument. Even such precious workhorse material as Pt is out of the question.

There are two main approaches to measure Seebeck effect in thermoelectric materials: integral and differential methods [24]. In the integral method, one end is maintained at a fixed temperature  $T_1$ , while another end is heated to induce, sometimes large, temperature gradient  $\Delta T = T_2 - T_1$ . According to the definition of Seebeck coefficient, we can write:

$$V_{TC} = V_T(T_1, T_2) - V_C(T_1, T_2) = \int_{T_1}^{T_2} (S_T(T) - S_C(T)) dT, \quad (2)$$

where  $V_T$  and  $S_T$  are, respectively, Seebeck voltage and Seebeck coefficient of the thermoelectrics, while  $V_C$  and  $S_C$  are those of connecting lead. Normally, these conductors are metals with low Seebeck coefficient, such as Cu or Pt with known thermoelectric properties. Thus, it is possible to infer Seebeck voltage of interest,  $V_T$ , from voltage measured,  $V_{TC}$  using the following expression:

$$V_{TC} + V_C(T_1, T_2) = V_T(T_1, T_2) = \int_{T_1}^{T_2} S_T(T) dT. \quad (3)$$

In the differential technique, small thermal gradient is used to estimate Seebeck coefficient at mean sample temperature. We can distinguish two approaches to this technique. In the DC method, constant thermal gradient is maintained, while mean temperature is varied, whereas in the AC method mean temperature is stabilized followed by the change in temperature gradient, usually in a sinusoidal form [25].

In the following, we describe a high-temperature homemade instrument to measure Seebeck coefficient with both integral and differential techniques. We based our design on the system described in Ref. [25], with some modifications, which are indicated below. Typical sample dimensions are pellets of around 10 mm diameter and 2 mm thickness, also ideal for laser flash measurements of thermal diffusivity.

**Figure 3** shows the design scheme of measurement. This instrument is composed of two thermocouples, two blocks of niobium (Nb), two cartridge heaters with built-in thermocouples and a radiation furnace with yet another thermocouple. The whole assembly is placed in a vacuum chamber equipped with turbo-pump station and operates in a vacuum of around  $7.5 \times 10^{-7}$  torr and between 300 and 950 K. Baseplate can be water-cooled. We now describe important components of the homemade system.

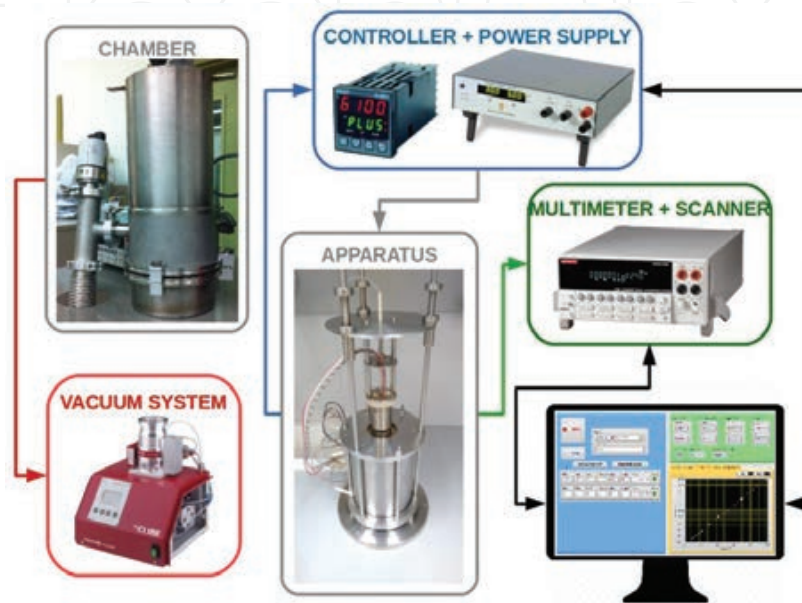


**Figure 3.** The top panel shows the main pieces of homemade instrument: vacuum chamber with turbo-pump station, furnace assembly and electronics for temperature control and voltage measurements. Screenshot of data acquisition software shows typical data resulting in differential AC measurement.

#### 2.4.3.1. Thermocouples

Thermocouples are used to measure both temperature of the sample at either side and Seebeck voltage. These consist of two different wires, one of chromel and another of niobium, of 0.1 mm diameter, inserted in a four-bore ceramic tube (1.2 mm diameter with 0.2 mm bores) in such a way that where these wires cross Nb ones make contacts with the sample [25]. Thus, the difference between temperature and voltage measurements is minimized to the diameter of Nb wire. These four-bore ceramic tubes are mounted on spring-loaded mechanisms to press them dynamically against the sample. Springs are located outside the hot-zone to maintain their elasticity. We found, that this system works well enough without the sophisticated strain gauge mechanism of Ref. [25]. Niobium is a good choice for its low Seebeck coefficient—we use two Nb leads to detect Seebeck voltage of the sample.

#### 2.4.3.2. Niobium blocks

Niobium blocks form the basis of apparatus. These cylinders, whose diameter and length are 20 mm, have two functions: they house cartridge heaters (and thus heat the sample differen-

tially) and thermocouples, and press the sample during the measurement. After finding copper to be a poor choice due to its reactivity, we chose niobium for its chemical inertness against typical thermoelectric materials and for its good thermal conductivity. An advantage of using a typical metallic block instead of a ceramic one, as in Ref. [25], is that they can act as a pair of electrical contacts, to inject electrical current in 4-probe resistivity measurement, while ohmic voltage can be measured on contacts used for Seebeck voltage. Metallic blocks are also easier to machine. These blocks are electrically insulated from the rest of the equipment by ceramic (MACOR<sup>®</sup>) collars and are pressed against the sample by two sets of three springs on support bars.

#### 2.4.3.3. Cartridge heaters

Cartridge heaters create controlled temperature gradient across the sample. They are inserted into niobium blocks off-center and are in good thermal contact with them. Cartridge heaters (from Watlow Ltd, 6.3 mm diameter, 25 mm length, 150 W) have individually incorporated J-type thermocouples. This enables us to smoothly control temperature gradient across the sample, even though cartridge heaters can deviate from the sample temperature by tens of degrees. We use programmable DC power supplies to control the temperature of cartridge heaters with high accuracy. Power supplies act as highly linear power amplifiers at the output of simple PID temperature controllers. Use of 0–5 V DC control logic helps us avoid introducing electronic noise into measurement, which would be rather troublesome in the typical solid state relay (SSR) scheme.

#### 2.4.3.4. Furnace

The sample and Nb-blocks are surrounded by a small tubular furnace to establish the average temperature and crucially to reduce radiative heat losses. Homemade furnace is composed of an aluminum oxide tube of 34 mm internal diameter with rolled-up Kanthal wire. This heating element is surrounded by mineral fiber and stainless steel sheet with low emissivity. After placing the sample between the Nb-blocks, the whole furnace can slide up on three steel posts to position.

#### 2.4.3.5. Breakout connector

The system has several thermocouples, and one of the crucial advantages of such an instrument, according to Ref. [25], is the possibility to easily swap and test different thermocouple wires for various samples. However, this poses technical challenge: these thermocouple wires must be run through the vacuum chamber. Although there exist commercial feedthroughs for thermocouples, these are costly and would eliminate flexibility to change the type of wire used. Therefore, we installed a break-out connector (DB-25) within the vacuum chamber and use copper wires from this post toward feedthrough (also DB-25, gold-plated pins) and outside toward electronics. As the break-out connector gets warm during operation (up to 80°C), we monitor its temperature with a resistive sensor (Pt100) and use this as “cold junction” in thermocouple measurements, in order to minimize spurious thermoelectric voltages.

#### 2.4.3.6. Electronics

Seebeck voltage, thermocouples monitoring the sample temperature and any resistance measurements (such as Pt100 of breakout connector or the sample itself) are measured by Keithley-2700 scanning multimeter. Other thermocouples (cartridge heaters, furnace) are connected to three West-P6100 PID controllers. Their 0–5 V DC programming output acts on DeltaES150 DC power supplies. Smooth voltage output reduces electronic noise on sensitive Seebeck voltage and resistivity measurements from heating system.

#### 2.4.3.7. Data acquisition and temperature set-point control

Data acquisition and temperature set-point control are handled by a LabVIEW program, which communicates via GPIB with multimeter and via RS485 serial protocol with PID controllers.

Salient features of this instrument are its operating range from slightly above room temperature up to 900 K and its flexibility to perform three different types of measurement schemes: quasi-integral, differential DC and differential AC. Each scheme has its own compromise between accuracy and overall required time for Seebeck coefficient measurements.

- **Quasi-integral** method is based on integral method and provides quick measurements, with low accuracy. We apply a step input to one heater, while the other is turned off. Although temperature of neither side of the sample is fixed, it is possible to extract the whole temperature-dependent Seebeck coefficient curve as polynomial function:

$$S(T) = S_0 + S_1 \cdot T + S_2 \cdot T^2 + S_3 \cdot T^3 + S_4 \cdot T^4 + S_5 \cdot T^5 + \dots \quad (4)$$

According to Eq. (3) Seebeck voltage is:

$$V_T(T_1, T_2) = S_0 \cdot (T_2 - T_1) + \frac{S_1}{2} \cdot (T_2^2 - T_1^2) + \frac{S_2}{3} \cdot (T_2^3 - T_1^3) + \frac{S_3}{4} \cdot (T_2^4 - T_1^4) + \dots \quad (5)$$

Therefore, from broad set of data,  $S_n$  polynomial coefficients can be numerically approximated. This technique does not generate particularly accurate results, but in as little as one hour, full  $S(T)$  curve may be obtained up to 900 K, which is very helpful for screening purposes, when faced with large number of samples. The peculiarity of this technique is that resulting  $S(T)$  curves are completely (and thus perplexingly) smooth, since they result from Eq. (4). Also, near the lowest and highest measured temperatures,  $S(T)$  curves behave anomalously due to the way the numerical fit works. In a sense, integral method is closest to real-life operation with large temperature differences present.

- **Differential DC** method is the closest to definition of Seebeck coefficient:

$$S(T) = \frac{dV}{dT} . \quad (6)$$

This method provides more accurate results than quasi-integral one, but is somewhat slower. We maintain more-or-less constant temperature gradient of a few degrees using cartridge heaters, while raising overall temperature smoothly with the furnace. This method also works without the surrounding furnace, but temperature differences between cartridge heaters and respective sample sides are quite large (several tens of degrees). It is also difficult to gauge any systematic errors arising from voltage and temperature offsets. Differential DC method is the closest operation mode to MMR system.

- *Differential AC* is the slowest method, but also the most accurate, as described in Ref. [25]. It takes several hours (easily a full day) to obtain a few Seebeck coefficient data points, for example, every 50 K. This is because furnace and cartridge heater temperatures must be stabilized first and this takes a long time at high temperatures, and then cartridge heater temperatures are oscillated (with a period of tens of minutes) to obtain complete data sets (e.g., in **Figure 4**). The great advantage of this method is that any voltage offsets arising from stray thermoelectric emfs or temperature offsets, for example, due to miscalibration of thermocouples, are eliminated by linear regression to collected data. Differential AC method is reminiscent of the operation mode of PPMS.

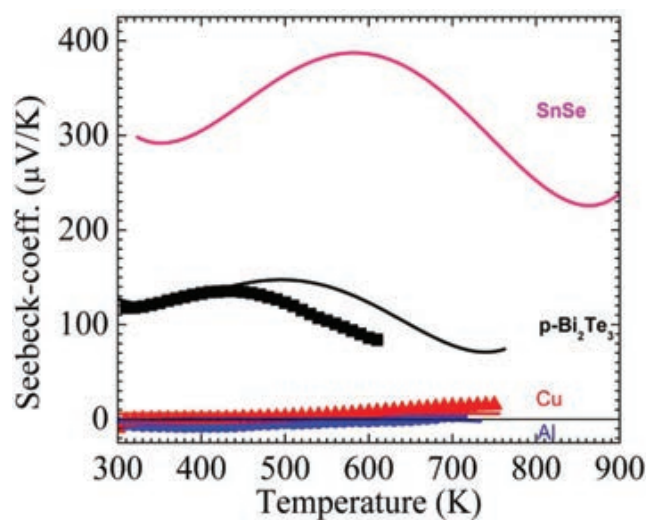


**Figure 4.** Typical temperature-dependent Seebeck coefficient data gathered with both differential DC method (full symbols) and integral method (lines) for low Seebeck metals, aluminum and copper, commercial p-type  $\text{Bi}_2\text{Te}_3$  ingot and test pellet of SnSe produced by arc-melting.

We end this section by presenting a few temperature-dependent Seebeck coefficient curves for test materials. We used pieces of commercial aluminum and copper to check effects of voltage and temperature offsets. These metals have minimal Seebeck coefficient values at room temperature, around  $3.5 \mu\text{V K}^{-1}$  for Al and  $6.5 \mu\text{V K}^{-1}$  for Cu. These would vary by only a few  $\mu\text{V K}^{-1}$  in the studied temperature range. We found, that differential DC method gives Seebeck coefficient values differing by less than  $10 \mu\text{V K}^{-1}$ , as absolute error. Relative error is less flattering, as for example, in the case of Al we measure negative values. Interestingly, integral method yields  $5\text{--}6 \mu\text{V K}^{-1}$  for Cu, very close to tabulated value. Nevertheless, instrument is designed to study thermoelectric materials with large Seebeck coefficient values. We can take

$\pm 10 \mu\text{V K}^{-1}$  as a rough estimate for systematic errors of the instrument. Results for commercial ingot of p-type  $\text{Bi}_2\text{Te}_3$  above  $100 \mu\text{V K}^{-1}$ , with characteristic maximum above 400 K, are similar to expected behavior. Finally, preliminary data from a pellet of  $\text{SnSe}$  produced by arc-melting and measured by quasi-integral method are also shown. These values are quite a bit lower than expected. The reason is still to be explored, but it is probably related to the fact, that data were recorded upon second heating run, and the sample may have suffered some chemical alteration. Whatever the case may be, it demonstrates the capabilities of the instrument.

#### 2.4.4. Thermal conductivity: laser flash thermal diffusivity method

So-called laser flash thermal diffusivity technique is a useful method to determine thermal properties of bulk samples and also thin films. This method allows measuring thermal diffusivity ( $\alpha$ ) of a sample in very broad temperature range (80–2500 K) and diffusivity (0.001–10  $\text{cm}^2/\text{s}$ ) range. For a given material,  $\alpha$  is directly related to the speed at which the material can change its temperature. Thus, thermal conductivity of the sample is obtained from measurements of diffusivity ( $\alpha$ ), specific heat ( $C_p$ ) and density ( $\rho$ ) of the sample by means of this relation:

$$\kappa = \alpha \cdot C_p \cdot \rho. \quad (7)$$

Commonly used systems, which measure  $\alpha$ , usually allow also measuring  $C_p$ . In spite of this feature, it is recommended to measure specific heat by means of a separate technique, like differential scanning calorimetry (DSC), in order to obtain more accurate estimation of the final value. However, at high temperature, where the specific heat reaches a constant value, diffusivity provides the essential parameter to estimate thermal conductivity.

As shown in **Figure 5a**, use of this method to measure  $\alpha$  implies illumination of one face of the sample by a laser pulse of length below 1 ms. An infrared (IR) detector placed behind rear face detects the signal, which is proportional to temperature rise. Thermal diffusivity value is obtained from IR signal rise against time. Example of IR signal profile vs. time is shown in **Figure 5b** corresponding to a graphite reference sample. Original Parker method [27] considers adiabatic conditions, and therefore, diffusivity value is obtained from thickness of the sample and time ( $t_{1/2}$ ), where IR signal profile reaches half of maximum rise:

$$\alpha = 0.1388 \left( \frac{L^2}{t_{1/2}} \right), \quad (8)$$

where  $L$  is the thickness of the sample. This method is valid only for adiabatic conditions; however, different methods have been designed in order to consider effects of finite laser pulse time and radiative losses in nonadiabatic conditions [27–30]. Correction fits and evaluation models based on this method are also provided by manufacturers of state-of-the-art thermal diffusivity measuring systems.

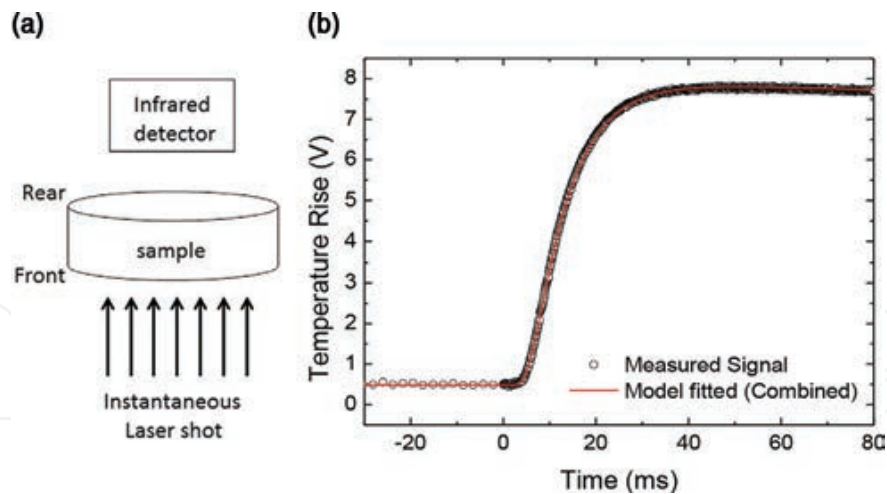


**Figure 5.** (a) Schematic illustration of laser flash method (adapted from *Thermoelectric Handbook: Macro to Nano*) [26], (b) signal profile and model fitted of graphite reference sample obtained in Laser flash system Linseis LFA 1000.

In addition, laser flash method imposes certain requirements on samples to be measured. It is mandatory to prepare plate samples with flat parallel planes to ensure correct acquisition of temperature profile at the rear face of the sample. Another important point about the sample preparation is to ensure the highest emissivity/absorption in the rear/front surface of the sample. For this purpose, thin coating of graphite well adhered over the sample's surface is commonly used (see **Figure 6a**).

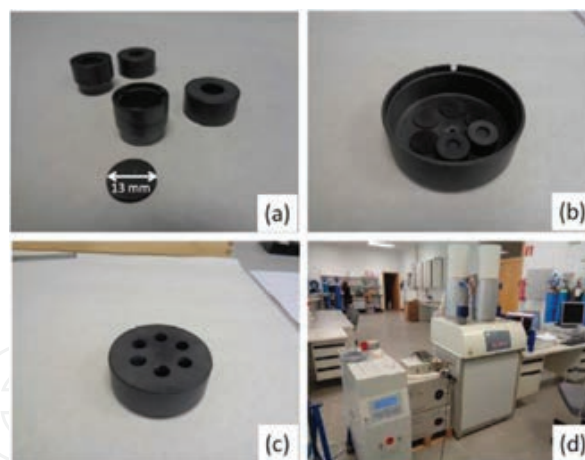


**Figure 6.** Different parts and sample holder (a, b), carousel for six samples (c), and general view of laser flash equipment: Linseis LFA 1000 (d).

#### 2.4.5. Thermal conductivity: $3\omega$ method

Alternative procedure to determine thermal conductivity is the so-called  $3\omega$  (3 omega) method [31]. We sandwiched a thin gold wire (diameter  $d = 25 \mu\text{m}$ ) between two identical, disk-shaped commercial  $\text{Bi}_2\text{Te}_3$  samples. We used BN spray to electrically insulate the wire from the sample. This is a slight variation in the original method as heating/sensing wire is

completely surrounded by the material. This method relies on applying AC current along the gold thread (heater) at frequency  $\omega$ , which generates thermal oscillations finally resulting in a voltage at the third harmonic ( $3\omega$ ), which is closely related to thermal conductivity ( $\kappa$ ):

$$V_{3\omega} = -\frac{V_{1\omega}^3 \cdot \beta}{8\pi \cdot l \cdot \kappa \cdot R_0} \cdot \left[ \ln(2\omega) + \ln\left(\frac{d^2}{4\alpha}\right) - 2 \cdot \ln(2) \right] - i \cdot \frac{V_{1\omega}^2 \cdot \beta}{16 \cdot l \cdot \kappa \cdot R_0}, \quad (9)$$

where  $V_{1\omega}$  is the amplitude of the ohmic voltage,  $l$  is the length of the heater,  $\beta$  is the temperature coefficient of gold,  $R_0$  is the nominal wire electrical resistance,  $\alpha$  is the thermal diffusivity of the sample. This formula is valid as long as thermal penetration depth,  $\sqrt{\alpha/2\omega}$  is greater than five times the wire radius. Performing linear fit to above expression, of  $V_{3\omega}$  vs  $\ln(2\omega)$ , thermal conductivity can be determined.

Here we present the results of this frequency-dependent third harmonic measurement for commercial p-type  $\text{Bi}_2\text{Te}_3$  at 300 K [31]. Performing linear fit to the expression indicated in this section, of  $V_{3\omega}$  vs  $\ln(2\omega)$ , as shown in **Figure 7**, thermal conductivity obtained is  $\kappa = 1.32 \text{ W m}^{-1} \text{ K}^{-1}$  at 300 K, matching reasonably well the results with TTO method of PPMS.

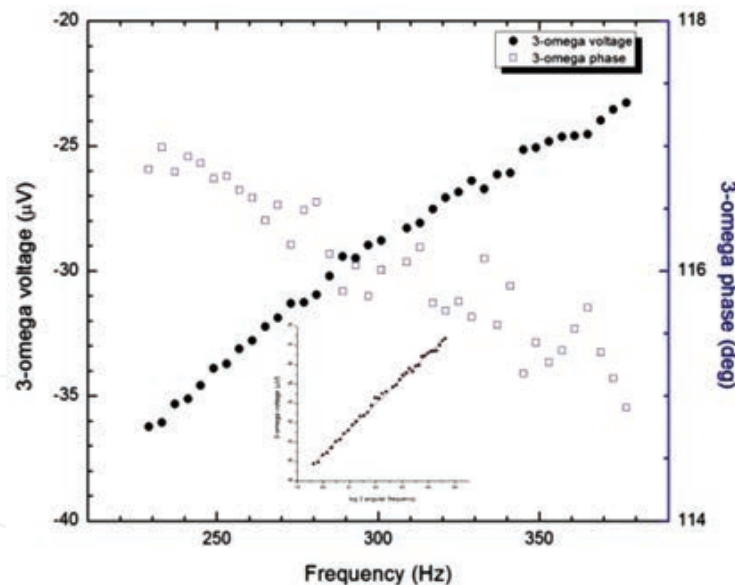


**Figure 7.**  $3\omega$  method for extracting thermal conductivity of commercial p-type  $\text{Bi}_2\text{Te}_3$  at room temperature, with frequency-dependent third harmonic voltage,  $V_{3\omega}$  (full symbols), and its phase shift (empty symbols) and with respect to logarithmic frequency (inset).

## 2.5. DFT calculations

We calculated the electronic density of states based on the experimentally determined unit cells in generalized gradient approximation (GGA) DFT scheme with Perdew-Burke-Emzerhof

(PBE) pseudopotentials in CASTEP using Materials Studio package [32, 33]. We considered  $1 \times 2 \times 2$  minimal supercells replacing between 0 and 4 Sn atoms with Ge or Sb out of 16. For Sb alloying, we also considered structures with one Sn atom missing. We checked two different configurations for each composition.

### 3. Results and discussion

#### 3.1. $\text{Bi}_2\text{Te}_3$

Pristine  $\text{Bi}_2\text{Te}_3$  was successfully prepared by arc-melting as reported in Ref. [20].  $\text{Bi}_2\text{Te}_3$  both n-type and p-type presents the best thermoelectric properties for applications near room temperature. Consequently, preparation of these compounds by arc-melting and verification of their thermoelectric properties was an interesting milestone. We found, that samples present high electrical conductivity, while they retain low thermal conductivity, which is strongly affected by morphology. On the other hand, Seebeck coefficient values are similar to previously reported results.

As shown in **Figure 8**, typical microstructure of samples can be described as piles of stacked sheets parallel to plane defined by **b** and **c** crystallographic axis, providing easy cleavage of materials. Thickness of individual sheets is well below  $0.1 \mu\text{m}$  (typically 20–40 nm). Thermoelectric properties of these materials are strongly influenced by this micro- or nanostructuration, involving many surface boundaries (interfaces) that are responsible for scattering of both charge carriers and phonons.

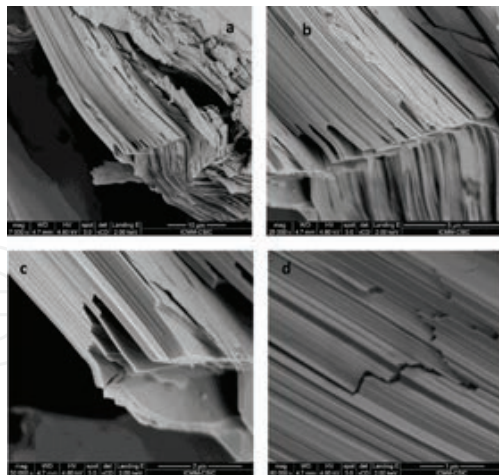


**Figure 8.** Typical microstructure of  $\text{Bi}_2\text{Te}_3$  prepared by arc-melting, showing nanostructuration in sheets perpendicular to crystallographic **c** axis. Magnification (a) 7000 $\times$ , (b) 25,000 $\times$ , (c) 50,000 $\times$ , and (d) 80,000 $\times$ .

Transport properties in pure  $\text{Bi}_2\text{Te}_3$  were measured in PPMS device [20] and high-temperature device (described in Section 2.4.3) on cold-pressed pellets. In the temperature range between 300 and 540 K, absolute value of Seebeck coefficient increases continuously until a maximum of  $-93 \mu\text{V K}^{-1}$ , as shown in **Figure 9a**. These measurements were repeated in different samples.

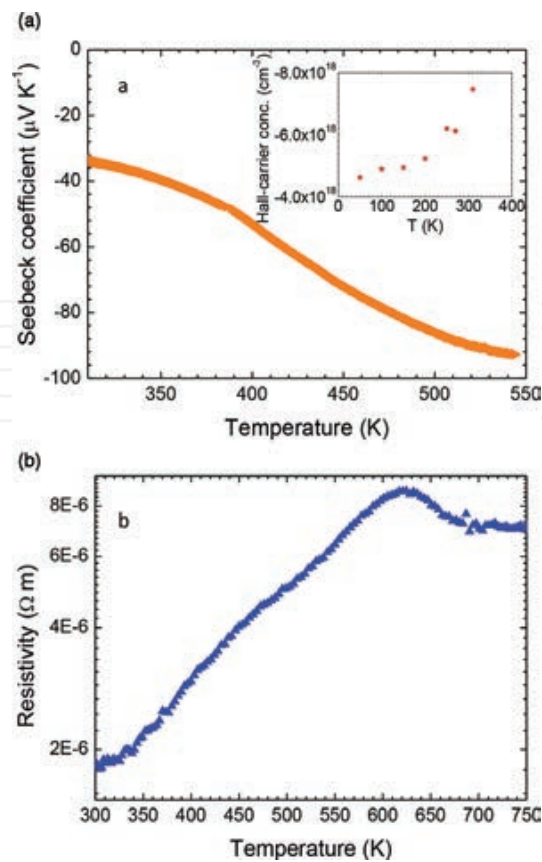


**Figure 9.** Temperature dependences of (a) Seebeck coefficient and (b) electrical resistivity of  $\text{Bi}_2\text{Te}_3$ , prepared by arc-melting.

Published data for undoped  $\text{Bi}_2\text{Te}_3$  offer a wide range of Seebeck coefficient values from  $-50$  to  $-260 \mu\text{V K}^{-1}$  [15, 34–36] depending on material's nature and charge carriers concentration. Compounds prepared by wet chemical methods demonstrate similar Seebeck coefficient values [18, 34], whereas for samples prepared by ball-milling and hot-pressing technique, this coefficient is as high as  $-190 \mu\text{V K}^{-1}$  [37]. In bismuth telluride samples, charge carriers concentration is strongly affected by antisite  $\text{Bi}_{\text{Te}}$  and  $\text{Te}_{\text{Bi}}$  defects, which are randomly created during synthesis process. This feature yields a wide range of Seebeck coefficient values measured in samples prepared by different methods [15, 34–39].

Electrical resistivity (**Figure 9b**) suggests semimetallic behavior, and, thus, we observe an increase in electrical resistivity with temperature. As temperature increases, charge carrier' scattering is augmented. We found resistivity values of  $2 \mu\text{Ohm m}$  at  $320 \text{ K}$ , whereas for samples prepared by mechanical alloying and SPS or hot pressing, they display higher values of  $30$  and  $7 \mu\text{Ohm m}$ , respectively [37, 38]. Samples synthesized by chemical processes show resistivity values between  $13$  and  $5 \mu\text{Ohm m}$  [34, 39]. These results indicate improvement compared to other preparation procedures. The number of thermally excited charge carriers increases with temperature, as shown by Hall concentration measurements. Charge carriers' density at  $310 \text{ K}$  is equal to  $7.46 \times 10^{18} \text{ cm}^{-3}$ , similar to other literature values [35]. Hall mobility of charge carriers is calculated by  $\mu_H = R_H \sigma$ , resulting in  $4514 \text{ cm}^2 \text{ V}^{-1} \text{ s}^{-1}$ , which is an extremely high value due to low resistivity. Preferred orientation of sheets might be the main cause of

this great electron mobility along measurement direction, resulting from the exceptionally anisotropic nature of  $\text{Bi}_2\text{Te}_3$ , with in-plane conductivity [40] over double that of out of plane.

Low thermal conductivity is critical for good thermoelectric performance. Thermal conductivity vs temperature is displayed in **Figure 10a** for  $\text{Bi}_2\text{Te}_3$ . At 365 K, thermal conductivity reaches its minimum value of  $1.2 \text{ W m}^{-1} \text{ K}^{-1}$  after decreasing along the whole temperature range. This is an excellent value for  $\text{Bi}_2\text{Te}_3$  bulk material, comparable to one of the lowest values presented in literature of  $0.9 \text{ W m}^{-1} \text{ K}^{-1}$ , Ref. [15]. It implies good compromise with excellent electrical resistivity and its electronic contribution to thermal conductivity. Layered nanostructured morphology of pellets is probably playing important role in reducing thermal conductivity, where abundant grain boundaries along phonon path (between layers or block of layers) increase phonon scattering. This effect compensates for improved electrical resistivity. Other procedures leading to nanostructured samples, i.e., ball-milling and hot pressing, yield thermal conductivity value of  $1.2 \text{ W m}^{-1} \text{ K}^{-1}$  at 330 K [37], while for chemical synthesis values of  $0.8 \text{ W m}^{-1} \text{ K}^{-1}$  at 380 K are obtained [34], however, in alloys with higher electrical resistivity. Eventually, then, our arc-melting technique produces  $\text{Bi}_2\text{Te}_3$  with ZT approaching 0.3 (**Figure 10b**).

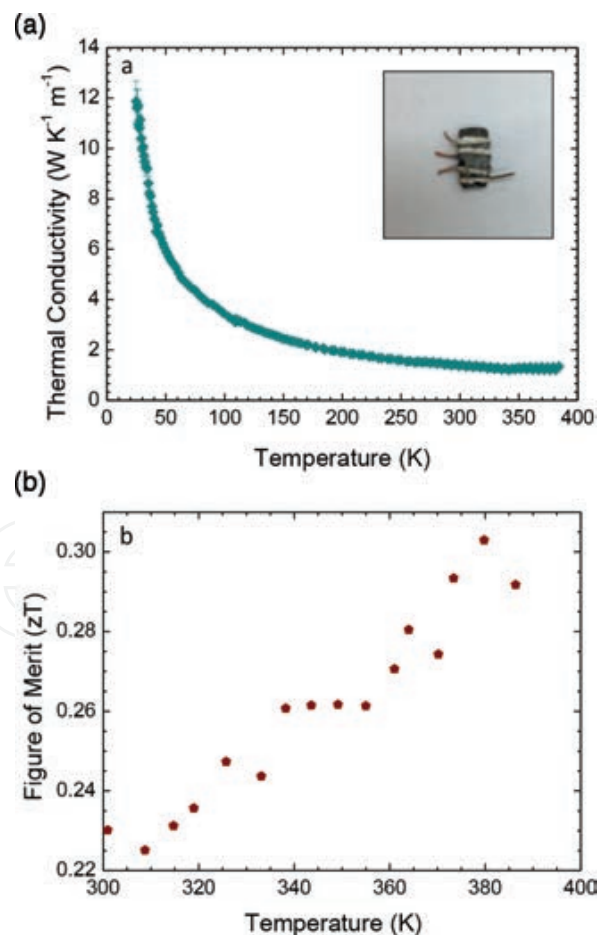


**Figure 10.** (a) Thermal conductivity measured in PPMS device; inset shows pellet used with TTO setup and (b) figure of merit of  $\text{Bi}_2\text{Te}_3$  prepared by arc-melting.

### 3.2. Bi<sub>2</sub>Te<sub>3</sub> based alloys: Bi<sub>2</sub>(Te<sub>1-x</sub>Se<sub>x</sub>)<sub>3</sub>

Preparation of Bi<sub>2</sub>Te<sub>3</sub>-Bi<sub>2</sub>Se<sub>3</sub> solid solutions by alloying Bi<sub>2</sub>Se<sub>3</sub> with Bi<sub>2</sub>Te<sub>3</sub>, where stronger Se-Bi interactions are created, enlarges band-gap energy and forms new donor levels. This may lead to enhanced electrical conductivity [41–43] and improve thermoelectric performance. Besides, decrease in lattice thermal conductivity is expected due to point defects induced by alloying. On the other hand, Bi<sub>2</sub>(Te<sub>1-x</sub>Se<sub>x</sub>)<sub>3</sub> alloys are extremely susceptible to anisotropic effects, which have been notable disadvantages in preparation of bulk samples that have not been able to keep high electrical resistivity. Attempts for preparation of oriented grains in bulk samples have been made to overcome this issue [44].

We prepared Bi<sub>2</sub>(Te<sub>0.8</sub>Se<sub>0.2</sub>)<sub>3</sub> pellets by arc-melting. NPD study was essential to investigate structural details of this doped sample. Neutrons are particularly suitable to study these intermetallic alloys having texturized nature of powder, which gives XRD patterns with large and untreatable preferred orientation effects. Neutrons provide bulk analysis, with good penetration; also the way of filling sample holders, (vanadium cylinders), helps to reduce unwanted preferred orientation, which is additionally minimized by rotation of sample holders. Moreover, lack of form factors for neutrons as diffraction probe enables accessing remote regions of reciprocal space, thus yielding accurate anisotropic displacement factors, which may give hints of the origin of phonon propagation across these materials, characterized by low thermal conductivity.

For Bi<sub>2</sub>(Te<sub>0.8</sub>Se<sub>0.2</sub>)<sub>3</sub>, NPD data were collected at RT at HRPT diffractometer of SINQ spallation source at PSI with  $\lambda = 1.494 \text{ \AA}$ . Crystal structure refinement was carried out in Bi<sub>2</sub>Te<sub>3</sub>-type model [45] in hexagonal setting of rhombohedral R-3m space group (no. 166),  $Z = 3$ , with Bi located at  $6c$  (00z) Wyckoff site and Te/Se distributed at random over two different crystallographic sites, (Te,Se)1 at  $3a$  positions and (Te,Se)2 at  $6c$ . There was excellent agreement between observed and calculated profiles, as shown in **Figure 11**; minor preferred orientation correction was effective in improving refinement for all reflections in the whole angular range, reaching low Bragg discrepancy factors of 5.15%. **Tables 1** and **2** include lattice and atomic parameters and anisotropic displacements factors, as well as discrepancy factors after refinement. Unit-cell parameters are  $a = 4.3315(1) \text{ \AA}$  and  $c = 30.208(7) \text{ \AA}$ . Unit-cell size is substantially smaller than that of parent Bi<sub>2</sub>Te<sub>3</sub> compound (with unit-cell parameters:  $a = 4.385915(6) \text{ \AA}$ ,  $c = 30.495497(1) \text{ \AA}$ , upon incorporation of smaller Se atoms.

**Figure 12** shows two views of refined crystal structure of Bi<sub>2</sub>(Te<sub>0.8</sub>Se<sub>0.2</sub>)<sub>3</sub>, along  $c$  axis (left panel) and perpendicular to  $c$  axis (right panel). It consists of hexagonal close-packed sheets, each layer being composed of fivefold stacking sequence of covalently bonded (Te,Se)2-Bi-(Te,Se)1-Bi-(Te,Se)2 atoms, whereas interatomic forces between adjacent layers ((Te,Se)2-(Te,Se)2 interactions) are mainly van der Waals type. As a consequence, crystals of these alloys are easily cleaved perpendicular to  $c$ -direction. Bi atoms are coordinated to 3 (Te,Se)1 at distances of  $3.129(7) \text{ \AA}$  and 3 (Te,Se)2 at  $3.102(9) \text{ \AA}$  in distorted octahedral configuration. Distance between terminal (Te,Se)2 of adjacent layers is  $3.634(9) \text{ \AA}$ . It is noteworthy that anisotropic displacement ellipsoids are strongly flattened with short axis perpendicular to bonding directions, i.e., along  $[110]$  directions as shown in the left panel in **Figure 12**.

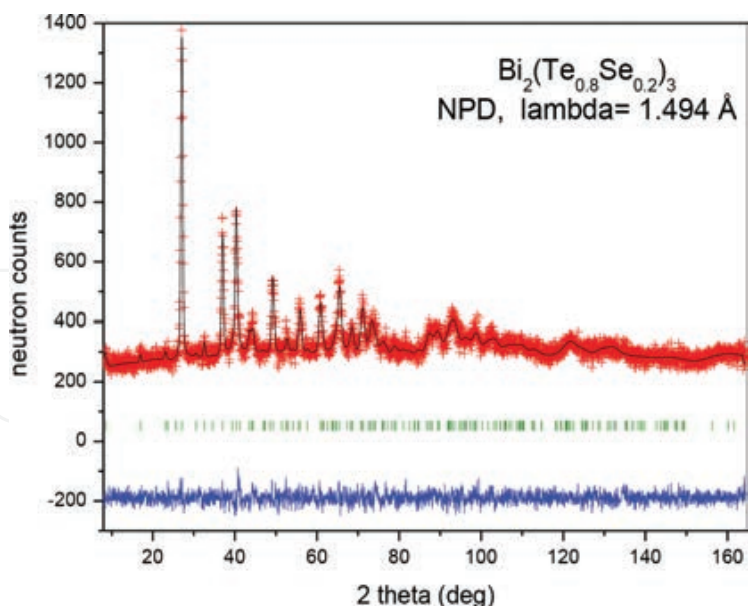


**Figure 11.** NPD profiles for  $\text{Bi}_2(\text{Te}_{0.8}\text{Se}_{0.2})_3$ . Crosses are experimental points, solid line is calculated fit and difference is at the bottom. Vertical marks correspond to allowed Bragg reflections.

	$x$	$y$	$z$	$U_{\text{eq}}$	Occupation (<1)
<b>Bi</b>	0.00000	0.00000	0.3956 (4)	0.010 (4)	
<b>Te1</b>	0.00000	0.00000	0.00000	0.025 (11)	0.80000
<b>Se1</b>	0.00000	0.00000	0.00000	0.025 (11)	0.20000
<b>Te2</b>	0.00000	0.00000	0.7897 (3)	0.017 (7)	0.80000
<b>Se2</b>	0.00000	0.00000	0.7897 (3)	0.017 (7)	0.20000

Unit-cell parameters:  $a = 4.3315$  (4) Å,  $c = 30.208$  (5) Å,  $490.83$  (10) Å<sup>3</sup>,  $Z = 3$ .  $U_{\text{eq}}$  and  $U^{\text{ij}}$  are, respectively, the equivalent and anisotropic atomic displacement parameters. Discrepancy factors after refinement are also included.

**Table 1.** Structural parameters for  $\text{Bi}_2(\text{Te}_{0.8}\text{Se}_{0.2})_3$  refined in R-3m space group (hexagonal setting) from NPD data collected at RT with  $\lambda = 1.494$  Å.

	$U^{11}$	$U^{22}$	$U^{33}$	$U^{12}$	$U^{13}$	$U^{23}$
<b>Bi</b>	0.009 (2)	0.009 (2)	0.010 (8)	-0.005 (2)	0.00000	0.00000
<b>Te1</b>	0.020 (6)	0.020 (6)	0.04 (2)	-0.010 (6)	0.00000	0.00000
<b>Se1</b>	0.020 (6)	0.020 (6)	0.04 (2)	-0.010 (6)	0.00000	0.00000
<b>Te2</b>	0.017 (5)	0.017 (5)	0.018 (12)	-0.008 (5)	0.00000	0.00000
<b>Se2</b>	0.017 (5)	0.017 (5)	0.018 (12)	-0.008 (5)	0.00000	0.00000

Discrepancy factors:  $R_p = 4.688\%$ ,  $R_{\text{wp}} = 5.895\%$ ,  $R_{\text{exp}} = 5.359\%$ ,  $R_{\text{Bragg}} = 5.151\%$ ,  $\chi^2 = 1.21$ .

**Table 2.** Anisotropic displacement parameters (Å<sup>2</sup>).

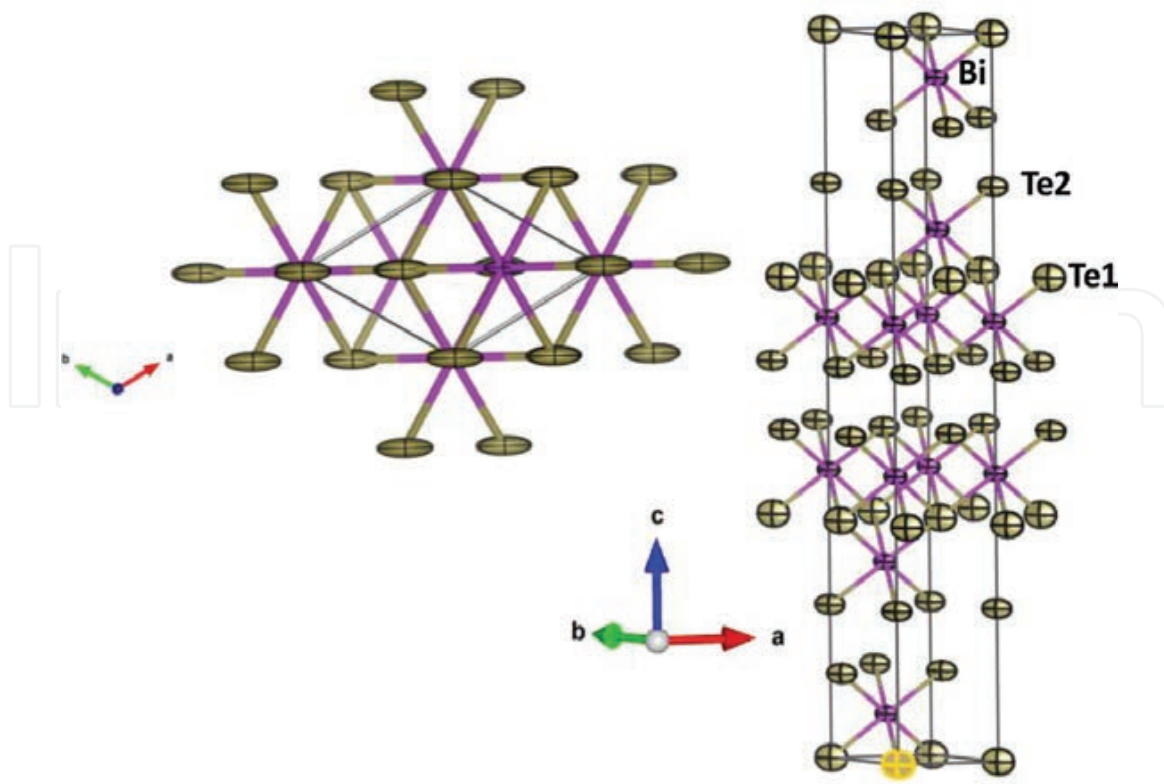


**Figure 12.** Two projections of crystal structure, along  $c$  axis (left panel) and perpendicular to  $c$  axis (right panel). Strongly anisotropic displacement ellipsoids (95% probability), with the short axis along  $[110]$  direction are illustrated.

Transport properties were evaluated in our homemade apparatus (Section 2.4.5). Seebeck coefficient vs temperature curve is plotted in **Figure 13a**.

Slow decrease in  $S$  is observed between 300 and 550 K, where average value is  $-75 \mu\text{V K}^{-1}$ . There is small improvement in thermopower regarding pure  $\text{Bi}_2\text{Te}_3$  samples, but it is still low in contrast to other  $\text{Bi}_2(\text{Te}_{1-x}\text{Se}_x)_3$  alloys, where values of  $-190 \mu\text{V K}^{-1}$  are reported [46] or even  $-259 \mu\text{V K}^{-1}$  at room temperature in samples with optimized composition [47]. Hall concentration of charge carriers is determined as  $3.1 \times 10^{19} \text{ cm}^{-3}$  at 300 K (inset in **Figure 13a**), which is somewhat higher than in pure  $\text{Bi}_2\text{Te}_3$  [20, 35], as a result of donor feature of  $\text{Bi}_2(\text{Te}_{1-x}\text{Se}_x)_3$  alloys.

As expected, temperature dependence of electrical resistivity (**Figure 13b**) exhibits the same semimetallic behavior as pure compound, but abrupt reduction in resistivity is observed at 530 K, until minimum value of  $55 \mu\text{Ohm m}$  is reached. Compared with pure compound (Section 3.1), with extremely low electrical resistivity ( $2 \mu\text{Ohm m}$  at 300 K) prepared by arc-melting, these results indicate deterioration of thermoelectric performance. The drop in electrical conduction is possibly a consequence of the enormous anisotropy of this alloy, meaning that orientations of layered structures are not aligned for improved electron mobility. Analogous relationship between charge carriers scattering, doping and electrical conductivity is reported by Ajay Soni et al. [47] for  $\text{Bi}_2\text{Te}_{2.2}\text{Se}_{0.8}$  nanocomposite, which shows metallic and semiconductor behavior throughout their measurement range with values around  $75 \mu\text{Ohm m}$  at room temperature.

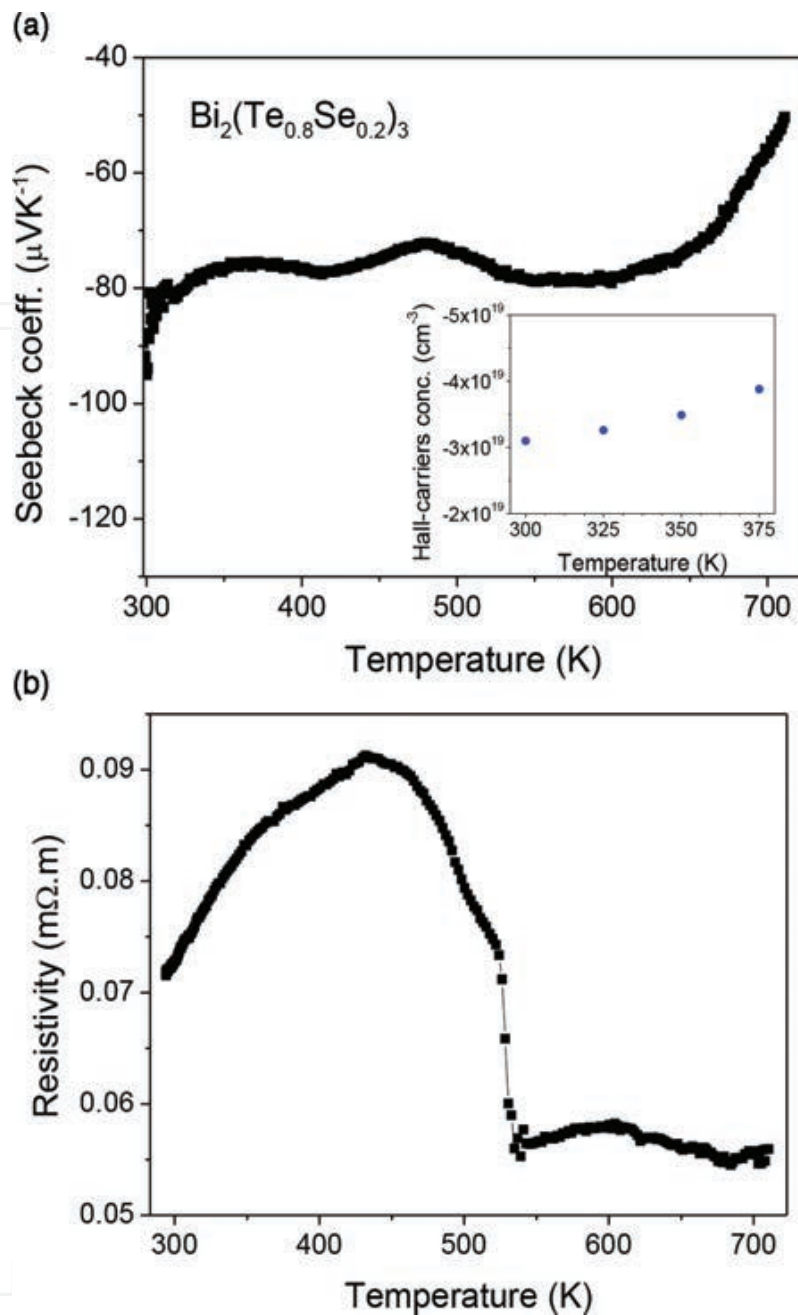


**Figure 13.** Temperature dependences of (a) Seebeck coefficient and (b) electrical resistivity for  $\text{Bi}_2(\text{Te}_{0.8}\text{Se}_{0.2})_3$  measured in homemade apparatus.

**Figure 14** shows dependence of total thermal conductivity on temperature determined in PPMS device.

Expected Umklapp maximum at low temperature appears with subsequent decrease over the whole measurement range until minimum value of  $0.8 \text{ W m}^{-1} \text{ K}^{-1}$  is reached at 300 K. This is better (lower) thermal conductivity than reported for pristine nanostructured  $\text{Bi}_2\text{Te}_3$  obtained by arc-melting, reaching  $1.2 \text{ W m}^{-1} \text{ K}^{-1}$  at 365 K [20]. Excellent present values could be related to stronger anisotropy, higher electrical resistivity and point defects induced by alloying. In  $\text{Bi}_2\text{Te}_3\text{-Bi}_2\text{Se}_3$  alloys produced by encapsulated melting and hot pressing, the best thermal

conductivity value was equal to  $1.04 \text{ W m}^{-1} \text{ K}^{-1}$  at 323 K [46], while for samples made by large-scale zone melting, values of  $1.2 \text{ W m}^{-1} \text{ K}^{-1}$  at 323 K are observed [48].

In samples prepared by polyol method followed by SPS, which leads to nanocomposite materials, low values of thermal conductivity are found:  $0.9 \text{ W m}^{-1} \text{ K}^{-1}$  at 300 K for  $\text{Bi}_2\text{Te}_{2.2}\text{Se}_{0.8}$  and  $0.7 \text{ W m}^{-1} \text{ K}^{-1}$  at 300 K for  $\text{Bi}_2\text{Te}_{2.7}\text{Se}_{0.3}$  nanocomposites [47]. The literature survey shows, that our thermal conductivity values are among the best reported, which is probably related to the nanostructuring effects, that we describe for arc-melted samples, with advantage of the simplicity of our one-step straightforward method.

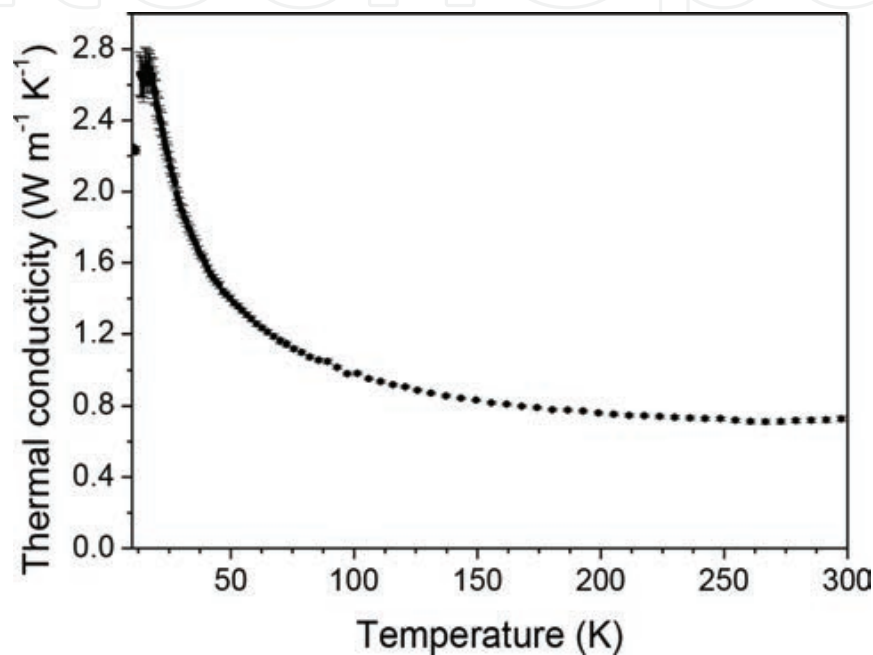


**Figure 14.** Temperature dependence of thermal conductivity of  $\text{Bi}_2(\text{Te}_{0.8}\text{Se}_{0.2})_3$  measured in PPMS device. Extremely low thermal conductivity of  $0.8 \text{ W m}^{-1} \text{ K}^{-1}$  is observed at 300 K.

### 3.3. SnSe and related alloys

Tin selenide and its various alloys show good thermoelectric performance at temperatures well above the maximum attainable in PPMS. Therefore, the main use of these results, measured with PPMS, is to guide us in search for candidate compositions. However, as we show, we found surprisingly high values of Seebeck coefficient, whereas thermal conductivity of tin selenide produced by arc-melting is considerably lower than that of single crystals. Both are highly promising results for thermoelectric materials.

#### 3.3.1. Structural characterization

We have prepared by simple and straightforward arc-melting technique highly textured SnSe samples with record Seebeck coefficient values and extremely low thermal conductivity [19]. Test NPD study was essential to investigate structural details of SnSe, since this bulk study is by far much less sensitive to the preferred orientation effects. Not only pristine SnSe, but other

several novel series of SnSe-based alloys, namely  $\text{Sn}_{1-x}\text{M}_x\text{Se}$  ( $M = \text{Sb}, \text{Ge}$ ) prepared by arc-melting, have been investigated by neutron diffraction. We will illustrate these studies with description of *in situ* structural evolution of  $\text{Sn}_{0.8}\text{Ge}_{0.2}\text{Se}$  in the temperature range of maximum thermoelectric efficiency. NPD data were collected in diffractometer D2B. Measurements were taken at 25, 200, 420 and 580°C.

**Figure 15** illustrates NPD patterns of  $\text{Sn}_{0.8}\text{Ge}_{0.2}\text{Se}$  at 420 and 580°C. Crystal structure can be Rietveld-refined in orthorhombic *Pnma* space group below 420°C. At this temperature, an orthorhombic (*Pnma*) to orthorhombic (*Cmcm*) phase transition takes place. **Figure 16** shows phase diagram displaying temperature dependence of unit-cell parameters of both orthorhombic phases. A dramatic rearrangement of atoms is observed along with phase transitions, bearing a more ordered structure. **Figure 17** displays crystal structures at room temperature, 200, 420 and 580°C. It is noteworthy, that change in displacement ellipsoids directions with temperature presents its largest axis along *c* direction in *Pnma* space group, while at high temperature it is oriented along *b* axis in *Cmcm* space group. In *Pnma*, structure consists of trigonal pyramids  $\text{SnSn}_3$  forming layers perpendicular to [100] direction, with thermal ellipsoids oriented within the layers, whereas across the transition to *Cmcm* the coordination environment changes to tetragonal pyramid, where large Sn ellipsoids in the basal square-plane adopt a configuration with the longest axis perpendicular to four closer chemical bonds, oriented along *b* axis of orthorhombic structure. Such high thermal displacements indicate strong rattling effect of Sn in a pentacoordinated cage, accounting for the observed decrease in thermal conductivity and good thermoelectric performance of this material.

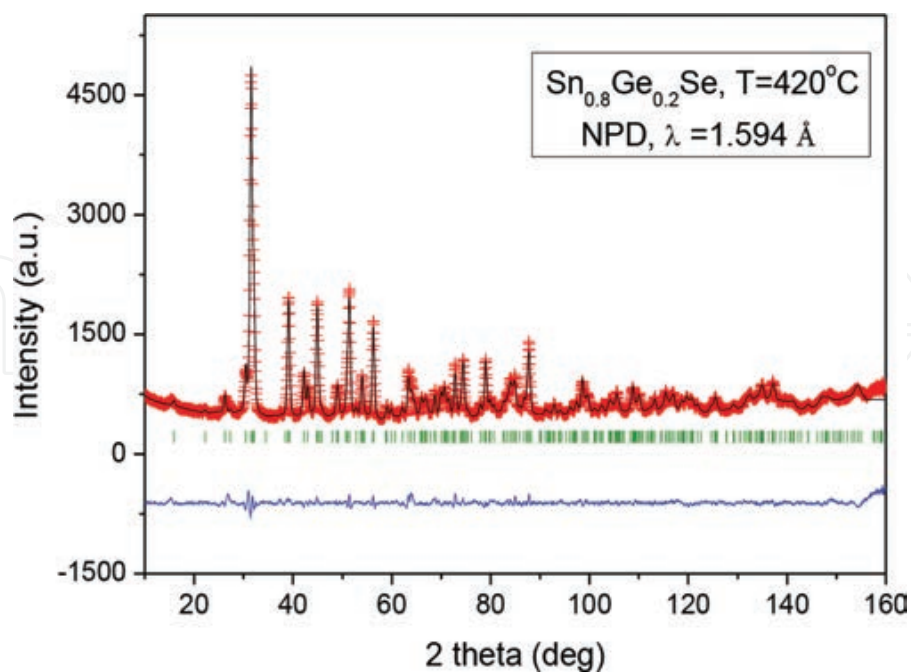


**Figure 15.** Observed (crosses), calculated (full line) and difference (at the bottom) NPD profiles for  $\text{Sn}_{0.8}\text{Ge}_{0.2}\text{Se}$  at 420 °C, just below the phase transition. Vertical markers correspond to allowed Bragg reflections.

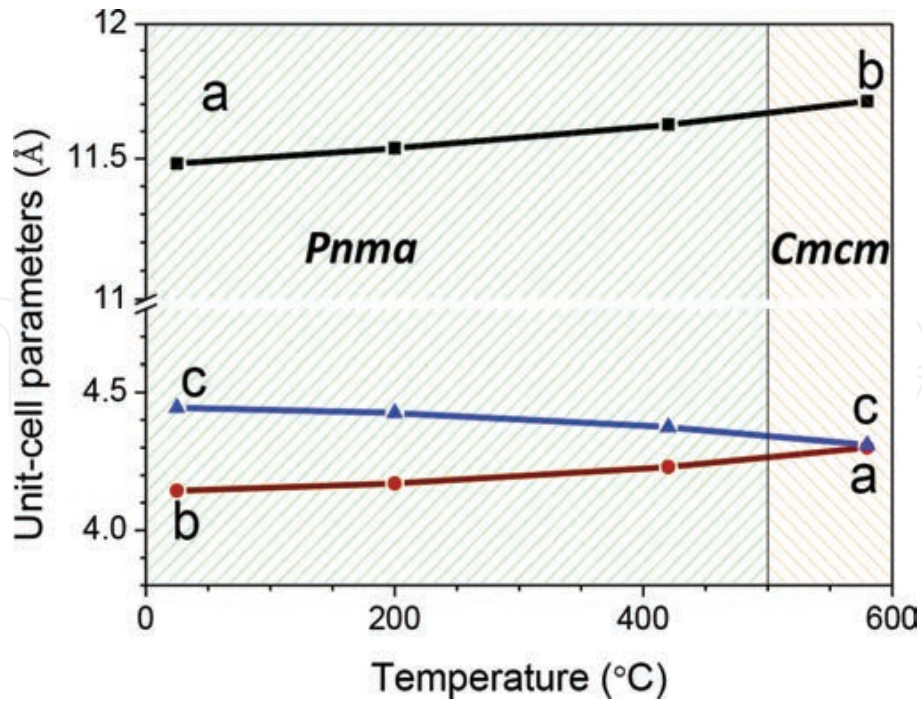


Figure 16. Phase diagram showing thermal evolution of unit-cell parameters.

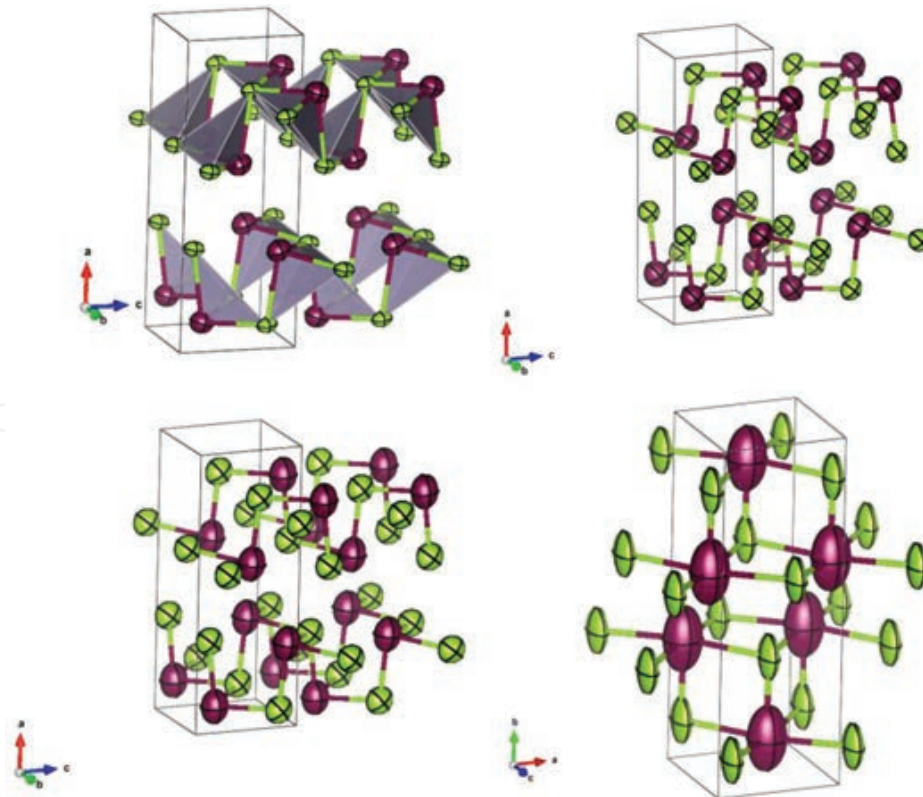


Figure 17. Crystal structures of orthorhombic phases at 25 (upper left), 200 (upper right), 420 (bottom left) and 580°C (bottom right).

### 3.3.2. Thermoelectric characterization

We first discuss our results on pure (i.e., unalloyed) SnSe, produced by arc-melting. The bar-shaped sample was cut directly from as-produced ingot as described above. **Figure 18** shows transport properties obtained in PPMS between 2 and 380 K. Seebeck coefficient (in middle panel) exhibits monotonic increase in positive (i.e., p-type) values reaching a maximum of  $668 \mu\text{V K}^{-1}$  [19]. At the time, this was the highest Seebeck coefficient value reported in SnSe. We have observed this behavior in various samples on repeated measurements, consistently. While preliminary studies reported values only around  $50 \mu\text{V K}^{-1}$  [49], the ground-breaking single crystal results of Zhao et al. [50] reach around  $580 \mu\text{V K}^{-1}$ , quite independent of crystallographic direction [50]. Meanwhile, other reported values of polycrystalline samples are close to this value [51–53]. Uncontrolled differences in hole concentration may play a role in these variations. Zhao et al. [50] found, that Seebeck coefficient value reaches its maximum in SnSe around 525 K. When we extrapolate our results (limited below 400 K in PPMS), we could expect as much as  $800 \mu\text{V K}^{-1}$ , and as we show below, indeed, we do find such high values with MMR device (described in Section 2.4.2).

Temperature dependence of electrical resistivity is shown in the bottom panel of **Figure 18**; Hall concentration of charge carriers at 300 K is  $7.95 \times 10^{15} \text{ cm}^{-3}$  [19]. Resistivity decreases exponentially with temperature, as expected for a semiconductor. We consistently find, that resistivity of SnSe and its alloys produced by arc-melting is rather high. This is a persistent problem of the technique, which we must address in the future. Nevertheless, we must also bear in mind, that these results from PPMS are limited to a temperature range well below that, where SnSe functions as a good thermoelectric. For comparison, our arc-melting produced pellet has bulk resistivity at room temperature (295 K) of around 64 mOhm m, significantly higher than expected: the single crystals of Zhao et al. [50] have 1 mOhm m within bc plane and 5 mOhm m along a-direction, whereas Sassi et al. [52] report 11 mOhm m along the pressing direction in polycrystals and 5 mOhm m perpendicular to it. Hall effect measurements at 300 K yields p-type hole concentration of  $7.95 \times 10^{15} \text{ cm}^{-3}$ . This is much lower than that of typical thermoelectrics and, indeed, of other SnSe reports (e.g.,  $4 \times 10^{17} \text{ cm}^{-3}$  by Zhao et al. [50]). Again, this is a persistent finding in our SnSe alloys: free charge carriers' concentration is much lower than expected, indicating the presence of strong traps for charge carriers. It also explains large electrical resistivity along with strong nanostructuring, producing abundant grain boundaries. Surprisingly, large Seebeck coefficient value is also related to low charge density, through Pisarenko relation [54].

Thermal conductivity of SnSe is shown in the top panel of **Figure 18**. It is overwhelmingly dominated by lattice contribution, due to low charge carriers' concentration.

Thermal conductivity peaks around 25 K due to Umklapp scattering and then starts to decrease monotonically throughout the measurement range, reaching a value as low as  $0.2 \text{ W m}^{-1} \text{ K}^{-1}$  at 395 K. This is a strikingly low value. Admittedly, direct heat-flow technique employed by PPMS is strongly affected by heat loss problems discussed above and these become acute above room temperature. Nevertheless, values are highly reliable below 100 K, and they are consistently very low there, too, in several samples. The intrinsic lattice thermal conductivity of SnSe is very low, probably an outcome of anharmonicity of chemical bonds. High Grüneisen

parameters and strong phonon-phonon interactions are expected as a result of the presence of lone-electron pairs of both  $\text{Se}^{2-}$  and  $\text{Sn}^{2+}$  ions [49, 55]. In fact, lone pairs of p-block elements play an important role deforming lattice vibration, which results in strong anharmonicity; significantly, anisotropic vibrations of both Sn and Se atoms are determined by NPD, with the main ellipsoid axes directed along chemical bonds (**Figure 17**), which is also indicative of such anharmonicity, as vibrations are hindered out of bonding direction by voluminous electron pairs filling empty space in the crystal structure. Moreover, thermal conductivity is significantly lower than those reported in single crystals ( $1.8 \text{ W m}^{-1} \text{ K}^{-1}$ ) [50, 56] and even lower compared to those recently reported for polycrystalline samples [52]. Extremely small values measured in the present material are most likely related to strong texture obtained during synthesis process, that leads to layered nanostructuring along *a* axis (**Figure 17**). This is particularly effective to boost phonon scattering at nanoscale, thus resulting in record low thermal conductivity for this polycrystalline material.

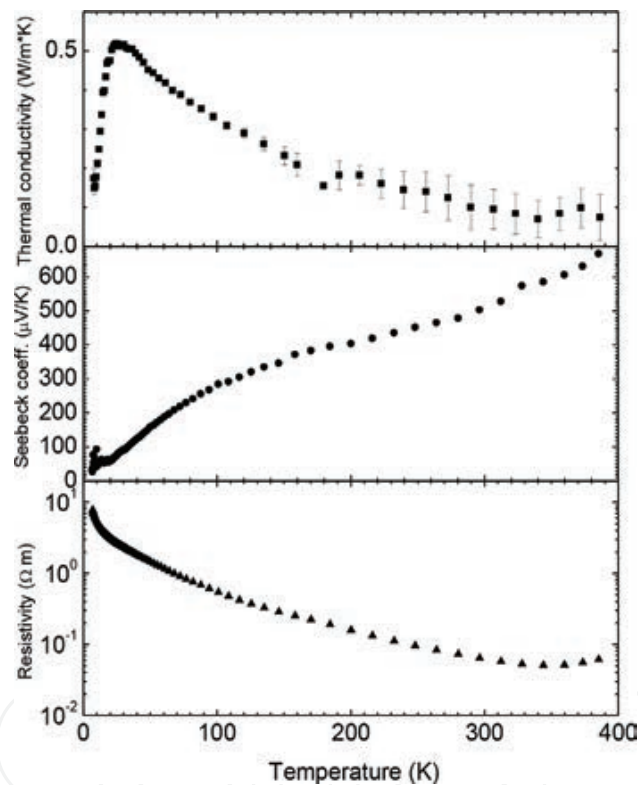


**Figure 18.** Temperature dependence of (top) thermal conductivity, (middle) Seebeck coefficient, (bottom) electrical resistivity of stoichiometric SnSe.

A second set of measurements of Seebeck coefficient at high temperature were carried out at MMR device, by comparing Seebeck effect of SnSe material with that of constantan wire, as described in Section 2.4.2. Seebeck coefficient was measured using  $1 \times 1 \times 8 \text{ mm}^3$  bar-shaped SnSe samples and reference constantan wire of 0.125 mm diameter. Reproducibility of measurements was confirmed by repeating them after making new contacts both on the sample and on reference constantan wire. This procedure warrants accuracy better than 5% over the whole temperature range.

**Figure 19** shows Seebeck coefficient as function of temperature  $S(T)$  measured using the method described above for SnSe. Initially,  $S(T)$  increases with  $T$  from room temperature up to 400 K, where it reaches about  $840 \mu\text{V K}^{-1}$ . Between 400 and 500 K, Seebeck coefficient is almost temperature independent, and above 500 K  $S(T)$  decreases monotonically up to the maximum experimental temperature, which is lower than temperature corresponding to structural transition from  $Pnma$  to  $Cmcm$ , described above from NPD data. These values are slightly higher than those reported by Zhao et al. [50] on single-crystalline samples. This enhancement can be related to nanostructuring of the sample and presence of high density of boundaries.

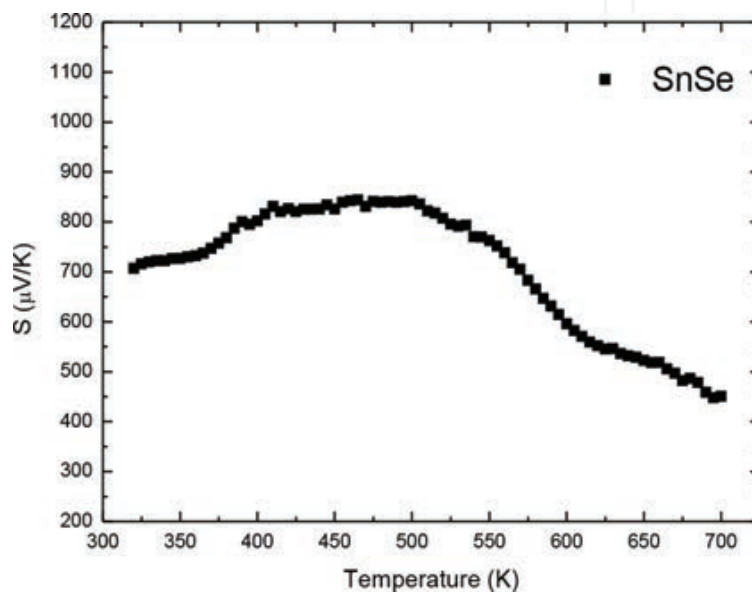


**Figure 19.** High-temperature Seebeck coefficient as function of temperature for SnSe measured in MMR device.

Morphology of the material produced by arc-melting is highly granular, nanostructured. This raises obvious concern about transport measurements. Do we measure intrinsic properties of the materials or are the data heavily distorted by grain-boundary effects? We can get an idea about this by comparing the three transport properties for the same material in two measurements. First, the sample is cut directly from the arc-molten ingot with a diamond saw and measured. Second, the material is directly cold-pressed after arc-melting and then measured. In both cases, the crystal structure, the platelet-like nanostructure and bulk bar-shaped form of samples are the same. What changes is the microstructure. The cold-pressed sample is denser with better grain-to-grain contacts. This is expected to raise both electrical and thermal conductivities. We use Sb-alloyed SnSe as an example. Thermal conductivity of SnSe and its alloys is not affected by the changed morphology. We also found that above room temperature, value of electrical resistivity has been improved by an order of magnitude, and Seebeck coefficient remains unchanged (not shown). This experiment demonstrates, that we are looking at the intrinsic thermal properties, whereas electrical connectivity of the material is in need of improving: measurements do not reflect the intrinsic electrical properties for tin selenide alloys.

Why would electrical and thermal conductivities respond differently to cold-pressing? Electrical conductivity is improved upon increasing grain-to-grain contacts and contact area. However, thermal conductivity is not affected. The reason is related to the nature of phonon scattering and the phonon mean-free path. We can estimate this by comparing low-temperature thermal conductivity (below Umklapp peak) and specific heat (inset in the top panel of **Figure 20**), using phenomenological relation for phonon diffusion:  $\kappa = \frac{1}{3}C_V \times v \times l$ , that relates thermal conductivity to specific heat at constant volume  $C_V$ , sound velocity ( $v$ ) and phonon mean-free path ( $l$ ). By ignoring the rather complex phonon dispersion of SnSe and using phonon velocities as given by Zhao et al. [50], we can estimate phonon mean-free path to be between 2 and 10 nm; effectively at low temperature, it is limited by the nanostructured grain-size, but at higher temperatures intrinsic properties dominate.

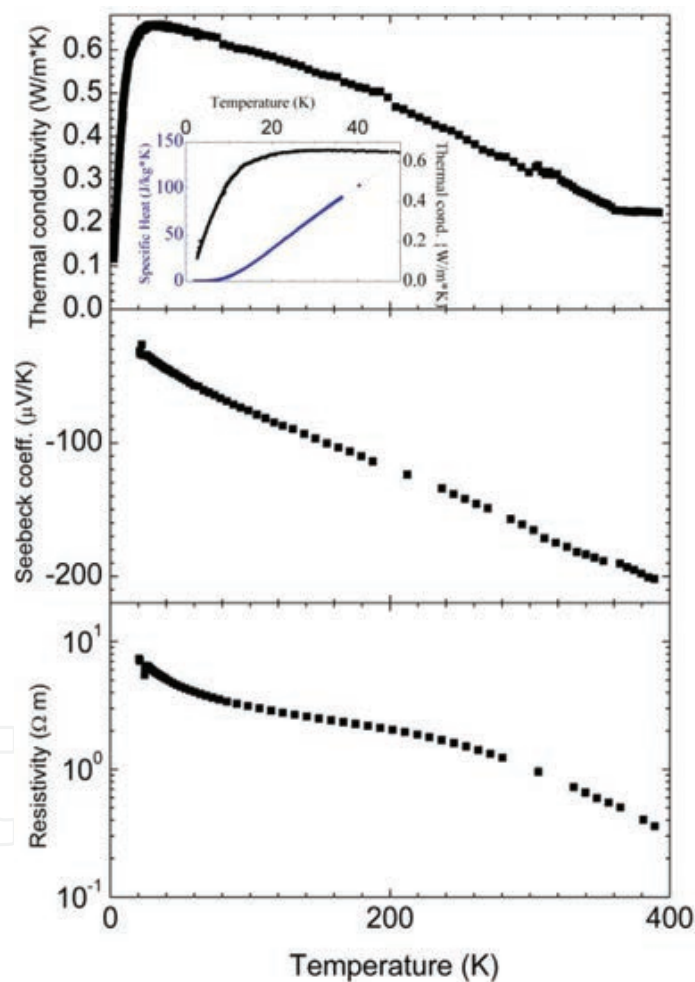


**Figure 20.** Temperature dependence of (top) thermal conductivity, (middle) Seebeck coefficient and (bottom) electrical resistivity and (inset) specific heat and thermal conductivity comparison at low temperature of  $\text{Sb}_{0.2}\text{Sn}_{0.8}\text{Se}$  alloy.

The idea to study alloys of SnSe with SbSe is to control Fermi level and concentration of free charge carriers. To our dismay, we found, that SnSbSe alloys display very high resistivity, higher even, than nominally stoichiometric SnSe, with very low Hall concentration of charge

carriers. We did manage to achieve n-type, negative, Seebeck coefficient. Indeed, absolute value of negative Seebeck coefficient reaches 100–200  $\mu\text{V K}^{-1}$ , depending on composition and temperature. These results are summarized for  $\text{Sb}_{0.2}\text{Sn}_{0.8}\text{Se}$  in **Figure 20**. Furthermore, for this composition, Hall effect measurements resulted in p-type, with hole concentration  $3 \times 10^{16} \text{ cm}^{-3}$  at room temperature. Expected free electron concentration, from *ab initio* calculations of electronic density of states (**Figure 21**), is around  $3 \times 10^{21} \text{ cm}^{-3}$  and obviously n-type for this level of Sb fraction in the compound. In order to resolve the apparent contradiction between measured and calculated free electron concentration and measured signs of Hall and Seebeck coefficients, we reconsidered the electronic structure calculation in view of strong Sn deficiency revealed by Rietveld refinement of NPD data. In our calculations, we use  $1 \times 2 \times 2$  minimal supercells with 16 Sn and 16 Se sites. Of these, we replace up to 3 Sn with Sb to approximate experimental alloying and remove one Sn to represent observed Sn site deficiency. Resulting band structure shows a striking narrow band in the gap above the valence band, appearing as a sharp peak in the density of states (DOS). This acts as shallow energy charge trap that localizes electrons transferred from Sb substitutes. Thus, Fermi level remains stuck in this band for a wide range of Sb concentration, invalidating our expectation of simple rigid-band charge transfer model. The complicated band structure is then responsible for different signs of Hall and Seebeck coefficients, too.

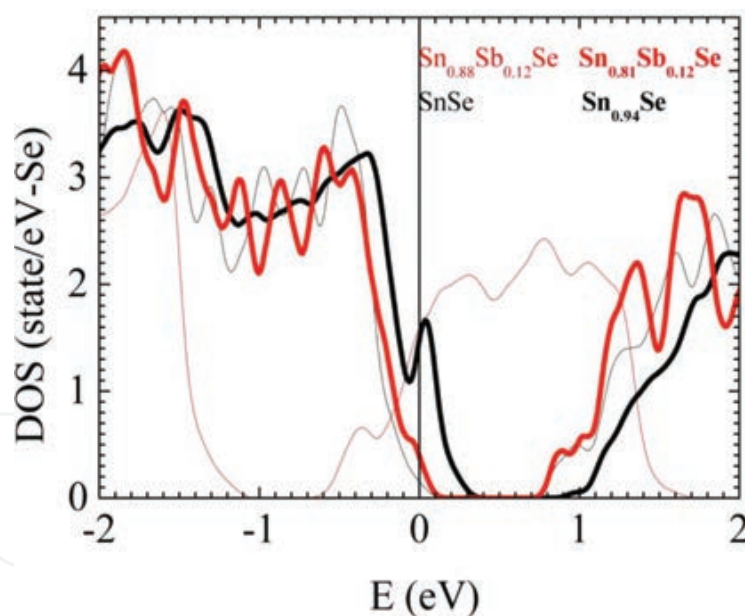


**Figure 21.** Electronic density of states of stoichiometric and Sn-deficient SnSe and Sb-SnSe with compositions indicated in labels. Fermi level is placed at  $E = 0$ , and thus band structures shift around with doping level.

The great advantage of arc-melting synthesis is that it affords a way to rapidly assay various compositions for thermoelectric properties. By introducing atoms of different radii, we can modify electronic structure, even without obvious charge transfer, this is so-called band engineering, for example, modification of bandwidth. Obvious candidates to do this are columnar neighbors of tin, lead and germanium. In the following we present results first on

SnPbSe alloys and then on SnGeSe alloys. In both series, we found p-type Seebeck coefficient values.

Studying three different SnPbSe alloy compositions with up to 30% Pb substitution on Sn site has shown no improvement on any of thermoelectric properties (**Figure 22**). Electrical resistivity increases by several orders of magnitude, as we have seen for SnSbSe alloys, too. Indeed, it is so high, that resistance of samples surpasses few MOhm limit of PPMS electronics at low temperature. The Seebeck coefficient value reaches up to  $600 \mu\text{V K}^{-1}$  at 400 K, which is high, but no higher, than in stoichiometric SnSe produced by arc-melting. Finally, thermal conductivity shows the same Umklapp peak at low temperature as SnSe and  $\text{Sb}_{0.2}\text{Sn}_{0.8}\text{Se}$  with no overall reduction.

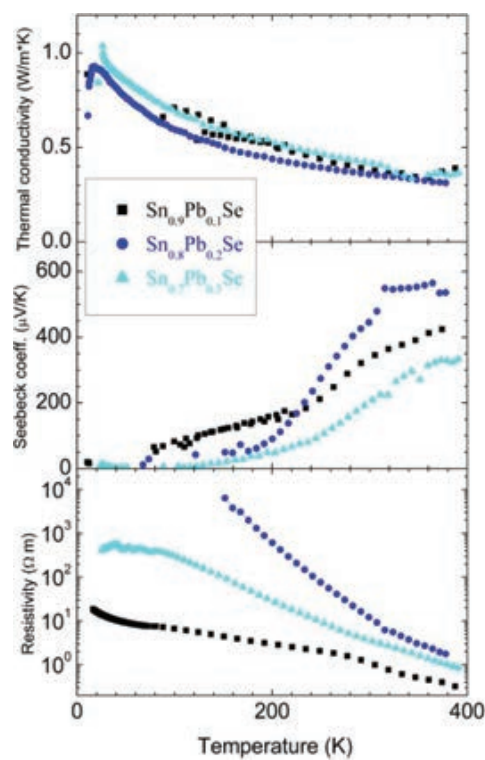


**Figure 22.** Temperature dependences of (top) thermal conductivity, (middle) Seebeck coefficient and (bottom) electrical resistivity of SnSe alloyed with Pb.

In contrast, by going to smaller ionic radius, SnGeSe alloy has several beneficial effects, although electrical resistivity is still too high. Most importantly, as shown in **Figure 23**, Seebeck coefficient value surpasses  $1000 \mu\text{V K}^{-1}$  for low GeSe fraction. Curious, nonmonotonic change of Seebeck coefficient with increase in GeSe fraction is supported by electronic structure calculations, based on experimentally determined crystal structures. These reveal, that semiconducting gap also varies nonmonotonously with Ge substitution, first increasing with respect to the gap of SnSe and then decreasing with more Ge (**Figure 24**). Large Seebeck coefficient value is caused partly by low charge carriers concentration, as indicated by resistivity, that is 1–2 orders of magnitude above that of stoichiometric SnSe, following Pisarenko relation.

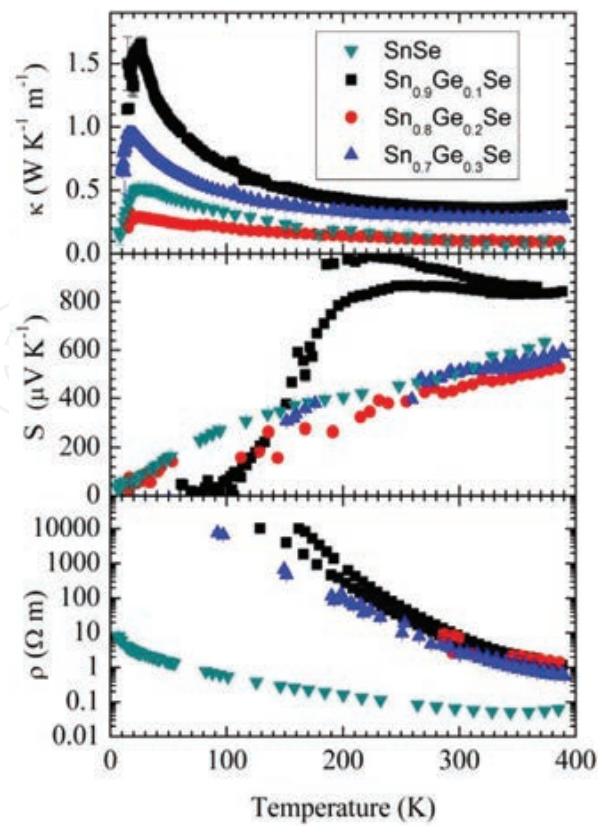


**Figure 23.**  $\text{Sn}_{1-x}\text{Ge}_x\text{Se}$  ( $x = 0, 0.1, 0.2, 0.3$ ) temperature dependences (top) thermal conductivity, (middle) Seebeck coefficient and (bottom) electrical resistivity—exhibiting characteristic semiconducting behavior. Two independent measurements are shown for  $x = 0.1$  and  $0.3$ . Below 150–200 K electrical resistance of Ge-doped SnSe samples increases beyond the limits (few MOhm) of the electronics of PPMS, and this influences Seebeck voltage, too (from Ref. [21]).

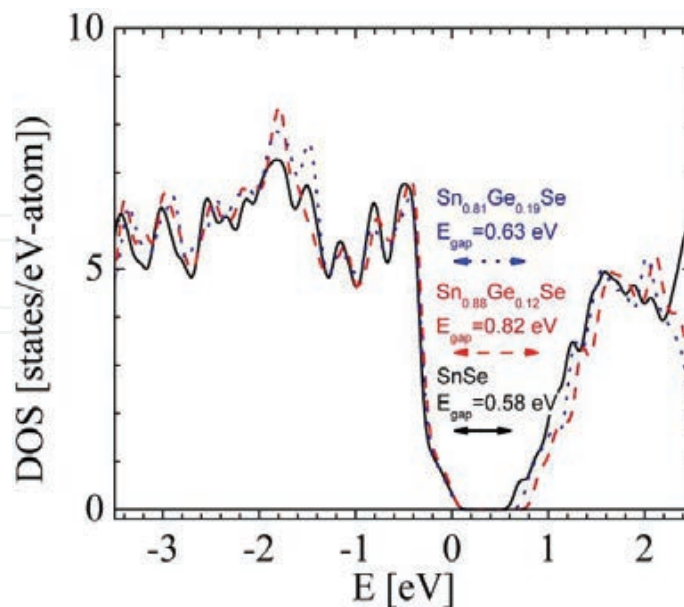


**Figure 24.** Calculated electronic density of states (DOS) of SnSe, black solid line,  $\text{Sn}_{0.88}\text{Ge}_{0.12}\text{Se}$ , red dashed line, and  $\text{Sn}_{0.81}\text{Ge}_{0.19}\text{Se}$ , blue dotted line (from Ref. [21]).

### 3.3.3. Thermal conductivity results from laser flash thermal diffusivity method

**Figure 25** shows total thermal conductivity ( $\kappa$ ) obtained by laser flash diffusivity method for different thermoelectric compounds: SnSe,  $\text{Sn}_{0.8}\text{Ge}_{0.2}\text{Se}$  and  $\text{Sn}_{0.8}\text{Sb}_{0.2}\text{Se}$ ; PbTe is used as a reference.

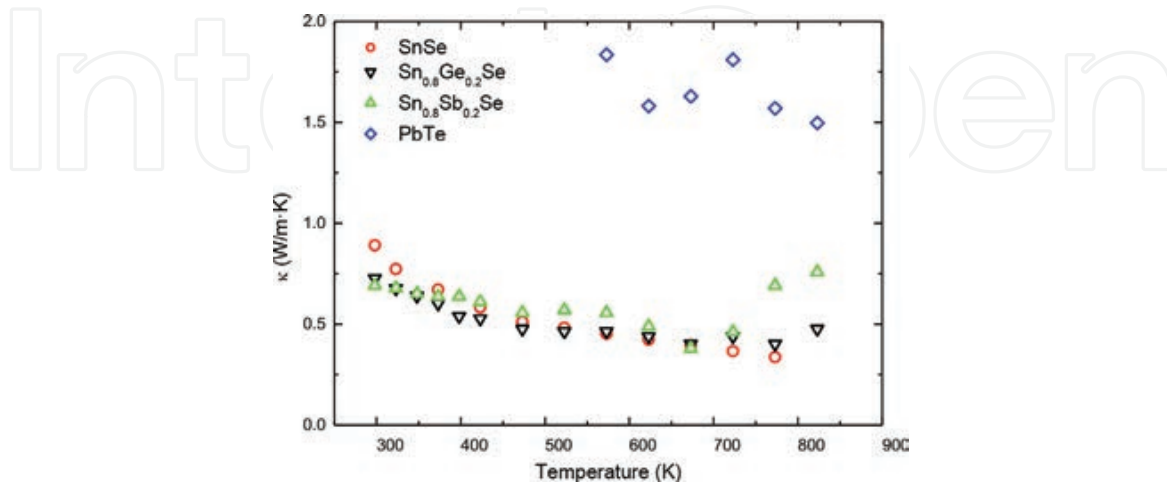


**Figure 25.** Thermal conductivity values of SnSe,  $\text{Sn}_{0.8}\text{Ge}_{0.2}\text{Se}$ ,  $\text{Sn}_{0.8}\text{Sb}_{0.2}\text{Se}$  and PbTe obtained by laser flash diffusivity method.

Lead telluride, PbTe, is a well-known thermoelectric material, that, due to its band gap of about 0.3 eV, is useful in intermediate temperature range of operation. Its thermal conductivity falls from room temperature with a  $1/T$  dependence, which is a fingerprint of the enhancement of phonon-phonon interactions with increasing temperature. This behavior, together with its band-gap value, makes PbTe one of the most competitive thermoelectric materials for generators above 500 K. However, several efforts are being made to enhance its efficiency. The main ways to drive this goal are enhancement of thermoelectric properties by nanostructuring and modifications in the density of states to create resonant states in the conduction band [57].

The pure SnSe and related alloys ( $\text{Sn}_{0.8}\text{Ge}_{0.2}\text{Se}$ ,  $\text{Sn}_{0.8}\text{Sb}_{0.2}\text{Se}$ ) display significantly lower thermal conductivities in the high-temperature region. At room temperature, values of total thermal conductivity are  $0.89$  and  $0.7 \text{ W m}^{-1} \text{ K}^{-1}$  for SnSe and  $\text{Sn}_{0.8}\text{Sb}_{0.2}\text{Se}$  compounds, respectively. These values are further reduced with increasing temperature, reaching  $0.4 \text{ W m}^{-1} \text{ K}^{-1}$  at 675 K. It is noteworthy, that above-described thermal conductivities determined in PPMS are considerably lower than values obtained by an indirect procedure, from thermal diffusivity.

Total thermal conductivity has two contributions, lattice thermal conductivity ( $\kappa_{lat}$ ), due to phonon transport, and charge carriers' thermal conductivity ( $\kappa_{ch}$ ), due to thermal transport of charge carriers (electrons and/or holes). As a first approximation, Wiedemann-Franz law [26] allows reasonable estimation of charge carriers thermal conductivity as a function of temperature,  $\kappa_{ch} = (L_0 T) / \rho$ , where  $L_0$  is the Lorentz number and  $\rho$  is the electrical resistivity. For the case of SnSe family, total thermal conductivity is almost fully dominated by lattice thermal conductivity. In fact, ratio of thermal conductivity due to charge carriers to total thermal conductivity is approximately  $10^{-4}$ . The different anisotropic direction of both measurements

might be related to the differences in the magnitude of determined thermal conductivity with respect to the direct measure provided by PPMS.

## 4. Conclusions

We have described a fast one-step procedure to prepare nanostructured intermetallic alloys belonging to the families of well-known  $\text{Bi}_2\text{Te}_3$  and recently described SnSe, all of them showing similar nanostructure consisting of stacks of nanosheets, that perturb propagation of phonons and provide extremely low thermal conductivity. Crystal structure studies from NPD data reveal anisotropic displacement parameters, probably due to the presence of lone-electron pairs of the p-block elements (Bi, Te, Sn, Se...) also contributing to low lattice thermal conductivity. Seebeck coefficient values are enhanced in SnSe system, reaching extraordinary high values close to  $1000 \mu\text{V K}^{-1}$  in SnGeSe alloys. As a drawback of nanostructuring, electrical resistivity values are much higher in this system than those described in single crystalline samples, probably arising from many grain boundaries, which perturb charge carriers path. We describe also a simple apparatus for the measurement of high-temperature transport properties, ideally conceived to determine  $S$  and  $\sigma$  in disk-shaped pellets directly obtained from the intermetallic ingots. The use of Nb pistons, chemically inert to reactive p elements like Bi, Te or Se, is particularly suitable given the weak  $S$  factor for Nb, yielding reproducible results for known materials like Cu or Al.

## Abbreviations

BN	Boron nitride
DFT	Density functional theory
GGA	Generalized gradient approximation
HRPT	High-resolution powder diffractometer for thermal neutrons
MMR	Micro-miniature refrigerator
NPD	Neutron powder diffraction
PBE	Perdue-Burke-Emzerhof
PSI	Paul Scherrer Institut
RT	Room temperature
SEM	Scanning electron microscope
SSR	Sum of squares regression
XRD	X-ray diffraction
ZT	Figure of Merit
CASTEP	Cambridge Serial Total Energy Package
PID	proportional-integral-derivative

## Acknowledgements

We thank the financial support of the Spanish Ministry of Science and Innovation to the project MAT2013-41099-R and by JCCM through Project PPII-2014-019-P. We thank the Institut Laue-Langevin (ILL) and Paul Scherrer Institut (PSI) for providing the neutron beam time.

## Author details

Federico Serrano-Sánchez<sup>1</sup>, Mouna Gharsallah<sup>1,2</sup>, Julián Bermúdez<sup>1</sup>, Félix Carrascoso<sup>1</sup>, Norbert M. Nemes<sup>1</sup>, Oscar J. Dura<sup>3</sup>, Marco A. López de la Torre<sup>3</sup>, José L. Martínez<sup>1</sup>, María T. Fernández-Díaz<sup>4</sup> and José A. Alonso<sup>1\*</sup>

\*Address all correspondence to: ja.alonso@icmm.csic.es

1 Institute of Materials Science of Madrid, Madrid, Spain

2 National School of Engineers, Sfax University, Tunisia

3 Department of Applied Physics and INEI, University of Castilla La Mancha, Ciudad Real, Spain

4 Institut Laue Langevin, Grenoble, France

## References

- [1] Funahashi R, Barbier T, Combe E.: Thermoelectric materials for middle and high temperature ranges. *J. Mater. Res.* 2015;30:2544–2557. doi:10.1557/jmr.2015.145
- [2] Zhang X, Zhao L-D.: Thermoelectric materials: energy conversion between heat and electricity. *J. Materiomics.* 2015;1(2):92–105. doi:10.1016/j.jmat.2015.01.001
- [3] Goldsmid HJ.: *Thermoelectric Refrigeration.* Springer, London; 1964. doi:10.1007/978-1-4899-5723-8
- [4] Rowe D.M., editor. *Thermoelectrics and Its Energy Harvesting.* CRC Press, Boca Raton, Florida; 2012.
- [5] Bell LE.: Cooling, heating, generating power, and recovering waste heat with thermoelectric systems. *Science.* 2008;321(5895):1457–1461. doi:10.1126/science.1158899
- [6] Zhao L-D, Dravid VP, Kanatzidis MG.: The panoscopic approach to high performance thermoelectrics. *Energy Environ. Sci.* 2014;7(1):251. doi:10.1039/C3EE43099E

- [7] Snyder GJ, Toberer ES.: Complex thermoelectric materials. *Nat. Mater.* 2008;7(2):105–114. doi:10.1038/nmat2090
- [8] Amatya R, Mayer PM, Ram RJ.: High temperature Z-meter setup for characterizing thermoelectric material under large temperature gradient. *Rev. Sci. Instrum.* 2012;83(7):075117. doi:10.1063/1.4731650
- [9] Chen G, Dresselhaus MS, Dresselhaus G, Fleurial J-P, Caillat T.: Recent developments in thermoelectric materials. *Int. Mater. Rev.* 2003;48:45–66. doi:10.1179/095066003225010182
- [10] Dresselhaus MS, Chen G, Tang MY, Yang R, Lee H, Wang D, et al.: New directions for low-dimensional thermoelectric materials. *Adv. Mater.* 2007;19(8):1043–1053. doi:10.1002/adma.200600527
- [11] Bilc DI, Hautier G, Waroquiers D, Rignanese G-M, Ghosez P.: Low-dimensional transport and large thermoelectric power factors in bulk semiconductors by band engineering of highly directional electronic states. *Phys. Rev. Lett.* 2015;114(13):1–5. doi:10.1103/PhysRevLett.114.136601
- [12] Wang Y, Huang H, Ruan X.: Decomposition of coherent and incoherent phonon conduction in superlattices and random multilayers. *Phys. Rev. B.* 2014;90(16):48–50. doi:10.1103/PhysRevB.90.165406
- [13] Mu X, Zhang T, Go DB.: Coherent and incoherent phonon thermal transport in isotopically modified graphene superlattices. *Carbon.* 2014;83:208–216. doi:10.1016/j.carbon.2014.11.028
- [14] Wang Y, Gu C, Ruan X.: Optimization of the random multilayer structure to break the random-alloy limit of thermal conductivity. *Appl. Phys. Lett.* 2015;106(7):073104. doi:10.1063/1.4913319
- [15] Lan Y, Minnich AJ, Chen G, Ren Z.: Enhancement of thermoelectric figure-of-merit by a bulk nanostructuring approach. *Adv. Funct. Mater.* 2010;20(3):357–376. doi:10.1002/adfm.200901512
- [16] Bomshtein N, Spiridonov G, Dashevsky Z.: Thermoelectric, structural, and mechanical properties of spark-plasma-sintered submicro- and microstructured p-type  $\text{Bi}_{0.5}\text{Sb}_{1.5}\text{Te}_3$ . *J. Electron. Mater.* 2012;41(6):1546–1553. doi:10.1007/s11664-012-1950-8
- [17] Cao YQ, Zhao XB, Zhu TJ, Zhang XB, Tu JP.: Syntheses and thermoelectric properties of  $\text{Bi}_2\text{Te}_3\text{Sb}_2\text{Te}_3$  bulk nanocomposites with laminated nanostructure. *Appl. Phys. Lett.* 2008;92(14):143106. doi:10.1063/1.2900960
- [18] Zhao Y, Dyck JS, Hernandez BM, Burda C.: Enhancing thermoelectric performance of ternary nanocrystals through adjusting carrier concentration. *J. Am. Chem. Soc.* 2010;132(14):4983–4983. doi:10.1021/ja100020m

- [19] Serrano-Sánchez F, Gharsallah M, Nemes NM, Mompeán FJ, Martínez JL, Alonso JA.: Record Seebeck coefficient and extremely low thermal conductivity in nanostructured SnSe. *Appl. Phys. Lett.* 2015;106(8):083902. doi:10.1063/1.4913260
- [20] Gharsallah M, Serrano-Sánchez F, Bermúdez J, Nemes NM, Martínez JL, Elhalouani F, et al.: Nanostructured Bi<sub>2</sub>Te<sub>3</sub> prepared by a straightforward arc-melting method. *Nanoscale Res. Lett.* 2016;11:142. doi:10.1186/s11671-016-1345-5
- [21] Gharsallah M, Serrano-Sánchez F, Nemes NM, Mompeán FJ, Martínez JL, Fernández-Díaz MT, et al.: Giant Seebeck effect in Ge-doped SnSe. *Sci. Rep.* 2016;6:26774. doi:10.1038/srep26774
- [22] Rodríguez-Carvajal J.: Recent advances in magnetic structure determination by neutron powder diffraction. *Phys. B.* 1993;192(1–2):55–69. doi:10.1016/0921-4526(93)90108-I
- [23] Borup KA, de Boor J, Wang H, Drymiotis F, Gascoin F, Shi X, et al.: Measuring thermoelectric transport properties of materials. *Energy Environ. Sci.* 2015;8:423–435. doi:10.1039/c4ee01320d
- [24] Martin J.: Protocols for the high temperature measurement of the Seebeck coefficient in thermoelectric materials. *Meas. Sci. Technol.* 2013;24:085601. doi:10.1088/0957-0233/24/8/085601
- [25] Iwanaga S, Toberer ES, Lalonde A, Snyder GJ.: A high temperature apparatus for measurement of the Seebeck coefficient. *Rev. Sci. Instrum.* 2011;83(6):063905. doi:10.1063/1.3601358
- [26] Rowe DM.: *Thermoelectrics Handbook: Macro to Nano.* Taylor & Francis ed. Boca Raton, FL: CRC Press; 2006. doi:10.1201/9781420038903
- [27] Parker WJ, Jenkins RJ, Butler CP, Abbott GL.: Flash method of determining thermal diffusivity, heat capacity, and thermal conductivity. *J. Appl. Phys.* 1961;32(9):1679–1684. doi:10.1063/1.1728417
- [28] Dusza L.: Combined solution of the simultaneous heat loss and finite pulse corrections with the laser flash method. *High Temp. High Press.* 1995;27–28(5):467–473.
- [29] Cowan RD.: Pulse method of measuring thermal diffusivity at high temperatures. *J. Appl. Phys.* 1963;34(4):926–927. doi:10.1063/1.1729564
- [30] Clark LM, Taylor RE.: Radiation loss in the flash method for thermal diffusivity. *J. Appl. Phys.* 1975;46(2):714–719. doi:10.1063/1.321635
- [31] Cahill DG.: Thermal conductivity measurement from 30 to 750 K: The 3 $\Omega$  method. *Rev. Sci. Instrum.* 1990;61(2):802–808. doi:10.1063/1.1141498
- [32] Clark SJ, Segall MD, Pickard CJ, Hasnip PJ, Probert MJ, Refson K, et al.: First principles methods using CASTEP. *Zeitschrift für Krist.* 2005;220(5–6):567–570. doi:10.1524/zkri.220.5.567.65075

- [33] Perdew JP, Burke K, Ernzerhof M.: Generalized gradient approximation made simple. *Phys. Rev. Lett.* 1996;77(18):3865–3868. doi:10.1103/PhysRevLett.77.3865
- [34] Saleemi M, Toprak MS, Li S, Johnsson M, Muhammed M.: Synthesis, processing, and thermoelectric properties of bulk nanostructured bismuth telluride ( $\text{Bi}_2\text{Te}_3$ ). *J. Mater. Chem.* 2012;22(2):725–730. doi:10.1039/C1JM13880D
- [35] Feng S-K, Li S-M, Fu H-Z.: Probing the thermoelectric transport properties of n-type  $\text{Bi}_2\text{Te}_3$  close to the limit of constitutional undercooling. *Chinese Phys. B.* 2014;23(11):117202. doi:10.1088/1674-1056/23/11/117202
- [36] Peranio N, Eibl O, Bäßler S, Nielsch K, Klobes B, Hermann RP, et al.: From thermoelectric bulk to nanomaterials: current progress for  $\text{Bi}_2\text{Te}_3$  and  $\text{CoSb}_3$ . *Phys. Status Solidi A.* 2015;11:1–11. doi:10.1002/pssa.201532614
- [37] Yang JY, Fan XA, Chen RG, Zhu W, Bao SQ, Duan XK.: Consolidation and thermoelectric properties of n-type bismuth telluride based materials by mechanical alloying and hot pressing. *J. Alloys Compd.* 2006;416(1–2):270–273. doi:10.1016/j.jallcom.2005.08.054
- [38] Zhao LD, Zhang B-P, Liu WS, Zhang HL, Li J-F.: Effects of annealing on electrical properties of n-type  $\text{Bi}_2\text{Te}_3$  fabricated by mechanical alloying and spark plasma sintering. *J. Alloys Compd.* 2009;467(1–2):91–97. doi:10.1016/j.jallcom.2007.12.063
- [39] Scheele M, Oeschler N, Meier K, Kornowski A, Klinke C, Weller H.: Synthesis and thermoelectric characterization of  $\text{Bi}_2\text{Te}_3$  nanoparticles. *Adv. Funct. Mater.* 2010;19(21):3476–3483. doi:10.1002/adfm.200901261
- [40] Ohsugi IJ, Kojima T, Sakata M, Yamanashi M, Nishida IA.: Evaluation of anisotropic thermoelectricity of sintered  $\text{Bi}_2\text{Te}_3$  on the basis of the orientation distribution of crystallites. *J. Appl. Phys.* 1994;76(4):2235–2239. doi:10.1063/1.357641
- [41] Scheele M, Oeschler N, Veremchuk I, Reinsberg KG, Kreuziger AM, Kornowski A, et al.: ZT enhancement in solution-grown  $\text{Sb}_{(2-x)}\text{Bi}_x\text{Te}_3$  nanoplatelets. *ACS Nano.* 2010;4(7):4283–4291. doi:10.1021/nn1008963
- [42] Sharp J, Goldsmid HJ, Nolas GS.: *Thermoelectrics: Basic Principles and New Materials Developments.* New York, NY: Springer; 2001. doi:10.1007/978-3-662-04569-5
- [43] Pei Y, Shi X, LaLonde A, Wang H, Chen L, Snyder GJ.: Convergence of electronic bands for high performance bulk thermoelectrics. *Nature.* 2011;473(7345):66–69. doi:10.1038/nature09996
- [44] Choi S-M, Lee KH, Lim YS, Seo W-S, Lee S.: Effects of doping on the positional uniformity of the thermoelectric properties of n-type  $\text{Bi}_2\text{Te}_{2.7}\text{Se}_{0.3}$  polycrystalline bulks. *J. Korean Phys. Soc.* 2016;68(1):17–21. doi:10.3938/jkps.68.17
- [45] Adam A.: Rietveld refinement of the semiconducting system  $\text{Bi}_{2-x}\text{Fe}_x\text{Te}_3$  from X-ray powder diffraction. *Mater. Res. Bull.* 2007;42(12):1986–1994. doi:10.1016/j.materres-bull.2007.02.027

- [46] Lee G-E, Eum A-Y, Song K-M, Kim I-H, Lim YS, Seo W-S, et al.: Preparation and thermoelectric properties of n-type  $\text{Bi}_2\text{Te}_{2.7}\text{Se}_{0.3}$ . *Dm. J. Electron. Mater.* 2015;44(6):1579–1584. doi:10.1007/s11664-014-3485-7
- [47] Ajay S, Zhao Y, Yu L, Michael Khor KA, Dresselhaus MS, Qihua X.: Enhanced thermoelectric properties of solution grown  $\text{Bi}_2\text{Te}_{3-x}\text{Se}_x$  nanoplatelet composites. *Nano Lett.* 2012;12:1203–1209. doi:10.1021/nl2034859
- [48] Wang S, Li H, Lu R, Zheng G, Tang X.: Metal nanoparticle decorated n-type  $\text{Bi}_2\text{Te}_3$ -based materials with enhanced thermoelectric performances. *Nanotechnology.* 2013;24(28):285702. doi:10.1088/0957-4484/24/28/285702
- [49] Patel TH, Vaidya R, Patel SG.: Effect of pressure on electrical properties of  $\text{SnS}_x\text{Se}_{1-x}$  single crystals. *High Press. Res.* 2003;23(4):417–423. doi:10.1080/0895795031000114368
- [50] Zhao L-D, Lo S-H, Zhang Y, Sun H, Tan G, Uher C, et al.: Ultralow thermal conductivity and high thermoelectric figure of merit in SnSe crystals. *Nature.* 2014;508(7496):373–377. doi:10.1038/nature13184
- [51] Chen C-L, Wang H, Chen Y-Y, Day T, Snyder J. Thermoelectric properties of p-type polycrystalline SnSe doped with Ag. *J. Mater. Chem. A.* 2014;2(29):11171–11176. doi:10.1039/c4ta01643b
- [52] Sassi S, Candolfi C, Vaney JB, Ohorodniichuk V, Masschelein P, Dauscher A, et al.: Assessment of the thermoelectric performance of polycrystalline p-type SnSe. *Appl. Phys. Lett.* 2014;104(21):212105. doi:10.1063/1.4880817
- [53] Fu Y, Xu J, Liu G-Q, Yang J, Tan X, Liu Z, et al.: Enhanced thermoelectric performance in p-type polycrystalline SnSe benefiting from texture modulation. *J. Mater. Chem. C.* 2016;4:1201–1207. doi:10.1039/C5TC03652F
- [54] Ioffe AF.: *Physics of Semiconductors*. New York, NY: Academic Press; 1960.
- [55] Katsuyama S, Maezawa F, Tanaka T.: Synthesis and thermoelectric properties of sintered skutterudite  $\text{CoSb}_3$  with a bimodal distribution of crystal grains. *J. Phys. Conf. Ser.* 2012;379(1):12004. doi:10.1088/1742-6596/379/1/012004
- [56] Stitzer DP.: Lattice thermal conductivity of semiconductors: a chemical bond approach. *J. Phys. Chem. Solids.* 1970;31:19–40. doi:10.1016/0038-1098(69)90198-7
- [57] Sootsman JR, Chung DY, Kanatzidis MG.: New and old concepts in thermoelectric materials. *Angew. Chem. Int. Ed.* 2009;48(46):8616–8639. doi:10.1002/anie.200900598